JGR Solid Earth

Key Points:

- We measure temperature, shear stress, and slip rate to assess energy dissipation during seismic slip in calcite-bearing fault materials
- Calcite decarbonation compensates frictional heat production in all tested fault materials
- Mechanical energy is dissipated for frictional heat in bare-rocks and for frictional heat and plastic deformation processes in gouges

Correspondence to:

S. Aretusini,
stefano.aretusini@ingv.it

Author Contributions:

Conceptualization: Stefano Aretusini, Elena Spagnuolo, Massimo Cocco
Data curation: Stefano Aretusini
Formal analysis: Stefano Aretusini
Funding acquisition: Carmen Vazquez, Massimo Cocco
Investigation: Stefano Aretusini, Arantzazu Nuñez Cascajero, Xabier Barrero Echevarria, Elena Spagnuolo
Methodology: Stefano Aretusini, Arantzazu Nuñez Cascajero, Xabier Barrero Echevarria, Alberto Tapetado
Project administration: Massimo Cocco
Resources: Carmen Vazquez

Mechanical Energy Dissipation During Seismic Dynamic Weakening in Calcite-Bearing Faults

Stefano Aretusini[1] , Arantzazu Nuñez Cascajero[2] , Chiara Cornelio[1] , Xabier Barrero Echevarria[2] , Elena Spagnuolo[1] , Alberto Tapetado[2] , Carmen Vazquez[2] , Giulio Di Toro[1,3] , and Massimo Cocco[1]

[1]Sezione di Sismologia e Tettonofisica, Istituto Nazionale di Geofisica e Vulcanologia, Rome, Italy, [2]Electronic Technology Department, Universidad Carlos III de Madrid, Leganés, Spain, [3]Dipartimento di Geoscienze, Università degli Studi di Padova, Padua, Italy

Abstract Earthquakes are frictional instabilities caused by the shear stress decrease, that is, dynamic weakening, of faults with slip and slip rate. During dynamic weakening, shear stress depends on slip, slip rate, and temperature, according to constitutive laws governing the earthquake rupture process. In the laboratory, technical limitations in measuring temperature during frictional instabilities inhibit the investigation and interpretation of shear stress evolution. Here we conduct high velocity friction experiments on calcite-bearing simulated faults, both on bare-rock and on gouge samples, at 20–30 MPa normal stress, 1–6 m/s slip rate and 1–20 m total slip. Seismic slip pulses are reproduced by imposing boxcar and regularized Yoffe slip rate functions. We measured, together with shear stress, slip, and slip rate, the temperature evolution on the fault by employing an innovative two-color fiber optic pyrometer. The comparison between modeled and measured temperature reveals that for calcite-bearing faults the heat sink caused by decarbonation reaction controls the temperature evolution. In bare-rocks, energy is dissipated as frictional heat, and temperature increase is buffered by the heat sink of the calcite decarbonation reaction. In gouges, energy is dissipated as frictional heat and for plastic deformation processes, balanced by the heat sink caused by the decarbonation reaction enhanced by the mechanochemical effect. Our results suggest that in calcite-bearing rocks, a common fault zone material for earthquake sources in the continental crust at shallow depth, the type of fault materials (bare-rocks vs. gouges) controls the energy dissipation during seismic slip.

Plain Language Summary During earthquakes, faults rocks lose strength, and therefore the ability to sustain shear stress as a consequence of slip, slip rate, and temperature resulting in dynamic weakening. The mathematical relationships between the decreasing strength and slip, slip rate, and temperature and the energy balance describing the partition of energy are of fundamental importance to model the propagation of an earthquake rupture. These relationships can be defined thanks to laboratory experiments that simulate seismic slip. Here, we tested calcite-bearing fault rocks simulated as bare-rock and gouges. During the experiments, temperature was monitored thanks to an innovative measuring system. Numerical models were done assuming all mechanical energy was converted into heat. By comparing all results above, we discovered that the mechanical energy in both bare-rocks and gouges is converted to heat but limited by the occurrence of endothermic decarbonation reaction. In gouges, also an energy contribution for plastic deformation processes is required. Our work implies significant changes in the commonly accepted energy budget for earthquake propagation and show the importance of slip rate and temperature in driving together the dynamic weakening during seismic slip.

1. Introduction

Seismic slip occurs with average slip rates of 1–10 m/s (Heaton, 1990) and is characterized by the decrease of shear stress from its peak to a residual value, defined as "dynamic weakening" or "dynamic breakdown" (see Cocco et al., 2023 and references therein). Dynamic weakening is associated with the earthquake shear stress (τ) drop and it is the stage in which slip rate (V) evolves reaching its peak (with a slip acceleration followed by deceleration) while slip (δ) increases, determining the slip rate time history (Kanamori & Brodsky, 2004). The shear stress evolution with coseismic slip is prescribed by constitutive laws usually adopted to simulate dynamic rupture propagation and arrest during an earthquake (Cocco et al., 2023; Ida, 1972; Ohnaka, 2013; Palmer & Rice, 1973 and references therein). Moreover, it is expected that during dynamic weakening temperature (T) also

increases by frictional sliding at the asperity (flash temperature) or bulk scale. Temperature is assumed to scale with the power dissipated in the slip zone (i.e., the rate of dissipated energy) as $T \propto \tau \times V$. The temperature increase during seismic slip triggers a series of processes spanning from phase transitions to chemical reactions that may decrease the effective normal stress at constant friction (thermal or thermochemical pressurization) or may decrease the fault frictional strength (e.g., flash heating, melt lubrication) (Beeler et al., 2008; Cornelio et al., 2022; Di Toro et al., 2011; Nielsen et al., 2021; Tullis, 2015). Laboratory experiments are playing a key role to progress in understanding dynamic weakening as well as to infer the processes governing shear stress evolution with time or slip, slip rate and temperature. In particular, high velocity friction experiments (HVFEs) show evident dynamic weakening of shear stress which is due to the combined contribution of high slip rates and temperature (Noda et al., 2011), sometimes yielding to a continuous weakening with increasing slip (Nielsen et al., 2021). In calcite-bearing rocks, calcite is expected to react and release CO_2 in the decarbonation reaction, that has an unknown effect on friction but might result in decreasing the effective normal stress via thermochemical pressurization, therefore contributing to dynamic weakening (Sulem & Famin, 2009). If thermochemical pressurization is inhibited by CO_2 drainage from the fault, dynamic weakening is controlled by viscous creep, active at extremely high temperature (>1,000°C) and shear strain rates (>10,000 1/s) (Aretusini, Núñez-Cascajero et al., 2021; Ashby & Verrall, 1973; J. Chen et al., 2021; De Paola et al., 2015; Pozzi et al., 2018, 2019, 2021).

Temperature rise is a clear evidence of energy dissipation as frictional heat both on- and off-fault but the exact contribution of frictional heat to the overall energy budget is still matter of debate (Kanamori & Heaton, 2000; Lambert & Lapusta, 2023). Constraining the frictional heat component of the dissipated energy would be beneficial to shed light on long-standing issues such as the stress drop scale invariance and energy density scaling (Cocco et al., 2023; Kanamori & Heaton, 2000). Moreover, constraining the part of the energy dissipated as frictional heat would allow to clarify the relationship between heat flow measurements of post-seismic temperature and the low absolute stress levels during seismic slip (Lambert & Lapusta, 2023). The total mechanical energy (named frictional work by Cocco et al. (2006)) dissipated in the fault zone during seismic faulting can be computed from the integral of shear stress evolution with coseismic slip from zero to the final slip value. It coincides with the total strain energy (elastic and gravitational) excluding the energy radiated by seismic waves (Cocco et al., 2023). The mechanical work is dissipated by many different processes occurring on- and off-fault, including the formation of new fractures, grain size reduction (i.e., comminution), leading to permanent (i.e., plastic) deformation of fault zone materials and frictional heat. Both grain size reduction and the temperature increase due to frictional heating contribute to the triggering of endothermic (or exothermic) reactions that may occur depending on the mineral assemblage of the fault zone (Nielsen et al., 2021). For carbonate bearing fault rocks, thermal decarbonation of calcite or dolomite is the dominant endothermic reaction (Sulem & Famin, 2009). For phyllosilicate bearing fault rocks, removal of interlayer water and thermal decomposition by dehydroxylation are the dominant reactions (Aretusini et al., 2019; Brantut et al., 2008; Ferri et al., 2011; Sulem et al., 2007; Veveakis et al., 2007).

By measuring the temperature changes independently of shear stress and slip rate, the contributions to the mechanical energy dissipation in the fault zone coming from heat and other thermally activated energy sinks could be constrained (Aubry et al., 2018). However, modeling the endothermal reactions requires knowledge of reaction kinetic laws which are poorly constrained at the extreme deformation conditions typical of seismic slip. In fact, the endothermal reactions are far from equilibrium and the reaction kinetic laws almost unknown, especially because amorphization or mechanical damage of the reagents may result in mechanochemical effects which lower the activation energy and change the mechanism of the reaction (Balaz, 2008; Hirono et al., 2013; Steinike & Tkáčová, 2000). Measuring temperature inside an experimental fault during experiments at stress and deformation conditions comparable to those occurring during earthquakes is technically challenging. Traditional methods, such as thermocouples which need to be in contact with the sample, are intrinsically limited in time and especially in space resolution and require that the temperature on the fault is inverted from a measurement occurring at several millimeters distance (Aubry et al., 2018; Woo et al., 2023). Instruments based on measuring the blackbody infrared radiation emitted from heated objects, such as infrared thermometers (Han et al., 2007) or pyrometers (Noda et al., 2011), were used mainly from outside the experimental fault, resulting in an underestimation of the temperatures reached inside the fault. Thermo-camera measurements, used to image the entire fault surface (Barbery et al., 2021), might instead result in a spatial averaging of the temperature measurements which could be lower than the actual ones (Núñez-Cascajero et al., 2021; Safarloo et al., 2023). Other methods to

quantify the heat would be measuring the evolution of the chemical structure of mineral reagents on the fault surface, defining the reaction kinetics and therefore the magnitude of the heat sinks. These measurements are not currently possible at the required time (<10–100 μs) and spatial resolution (asperity scale, <10–100 μm, Dieterich & Kilgore, 1994) of the processes governing dynamic weakening (Rice, 2006).

Here, we use rotary shear experiments to simulate the extreme deformation conditions during dynamic weakening occurring at seismic slip rates. We chose pure calcite-bearing rock and gouge samples as analogs of carbonate-bearing fault rocks. This choice was motivated by the abundancy of carbonatic rocks on Earth's crust at shallow depth in many seismically active areas worldwide. In fact, seismic sequences with M_w 6 mainshocks including 2009 l'Aquila (Chiarabba et al., 2009), 2008 Wenchuan (J. Chen et al., 2013), and 1995 Aigion (Bernard et al., 2006) occurred in fault systems hosted by carbonatic rocks. We impose on the experimental faults both boxcar and regularized Yoffe slip rate functions, which were proposed to be analog to slip rate functions during seismic slip (Harbord et al., 2021; Tinti et al., 2005). We present unique high spatial and temporal resolution on-fault microscale measurements of temperature evolution with slip and, building on our previous work (Aretusini, Núñez-Cascajero et al., 2021), we compare them to temperatures computed by numerical models. We highlight the importance of decarbonation heat sink to limit the temperature increase during dynamic sliding at seismic slip rates in calcite-bearing faults. Moreover, we show that in calcite-bearing faults the mechanical energy (or frictional work) is largely dissipated as (a) heat balanced by heat sinks (including decarbonation) in the case of bare-rocks and, (b) heat and energy for plastic deformation processes, balanced by heat sinks (including decarbonation) in the case of gouges. Our results suggest that the type of fault materials, that is, bare-rocks or gouges, influence how mechanical energy is dissipated during seismic slip. Finally, we directly provide independent measurements of temperature and velocity, laying the groundwork for understanding and quantifying the individual contribution of the two variables in controlling dynamic weakening. This relationship is only theoretical and the interdependency between temperature and velocity is not yet constrained.

2. Methods

2.1. SHIVA, Sample Preparation, and High Velocity Friction Experiments

We ran nine high velocity friction experiments (HVFEs) in the Slow to High Velocity Apparatus SHIVA (Di Toro et al., 2010). Here, we performed HVFEs on rock cylinders with bare surfaces in contact (i.e., bare-rocks) or gouge layers, which were positioned in SHIVA sample chamber (Figure 1a) thanks to specific sample holders (Figures 1b and 1c).

We prepared samples from Carrara marble rocks composed of ∼99 wt.% calcite, <1 wt.% quartz, with dolomite and white mica impurities (Violay et al., 2013). In each of the bare-rock HVFEs (Figure 1b), two samples consisting of hollow cylinders (30–50 mm inner-outer diameter, 50 mm height) were cored, glued with epoxy resin (Epofix Struers) to aluminum sleeves, and rectified with a lathe to obtain surface contact parallelism when installed in SHIVA (Nielsen et al., 2012). Then, we imposed on the rock surfaces #220 and #2000 roughness by wet sanding. On the sample that was positioned on the axial side during the experiment, we drilled a hole with diameter of 1–1.2 mm at ∼20.2 mm from the center of the sample to position a singlemode (SMF) and a multimode (MMF) optical fiber. The fibers tip had the core/cladding exposed so that it was positioned just at the same height of the sliding/contact surface. The fibers were glued to the hole with a heat resistant silicate glue (Everbuild®), stable up to 1,200°C. Before each experiment, both fibers were connected to a 650 nm light source to test for integrity and capability to transmit light. Moreover, a photo was acquired under a reflection microscope (DeltaPIX Modus6ZS-3D or Leica MZ9.5), to verify the capability to transmit light of both fibers. In particular, using a microscope was necessary to observe the lit up SMF fiber due to the very small core diameter of 10 μm. The photos allowed us to check both the radial and the vertical position: when the fiber tip was in focus together with the sample surface, it was considered at a distance of 0 ± 0.1 mm from the surface, due to uncertainty in the positioning of the fiber tip.

Carrara marble rock was ground and sieved below 250 μm grain size to obtain a granular fault gouge analog. In the gouge HVFEs (Figure 1c), the sample holder consisted in two hollow cylinders (13.9–30 mm inner-outer diameter), with a basal surface meshed with a 0.7 × 0.7 × 0.2 mm pattern. This pattern was on the surface on which the gouge layer was placed. The sample holder installed on the axial column had an access hole to the surface, in which the two SMF and MMF fibers were installed before each experiment and checked for focusing-positioning and transmission with a similar method as above, but referred to the part of the axial sample holder
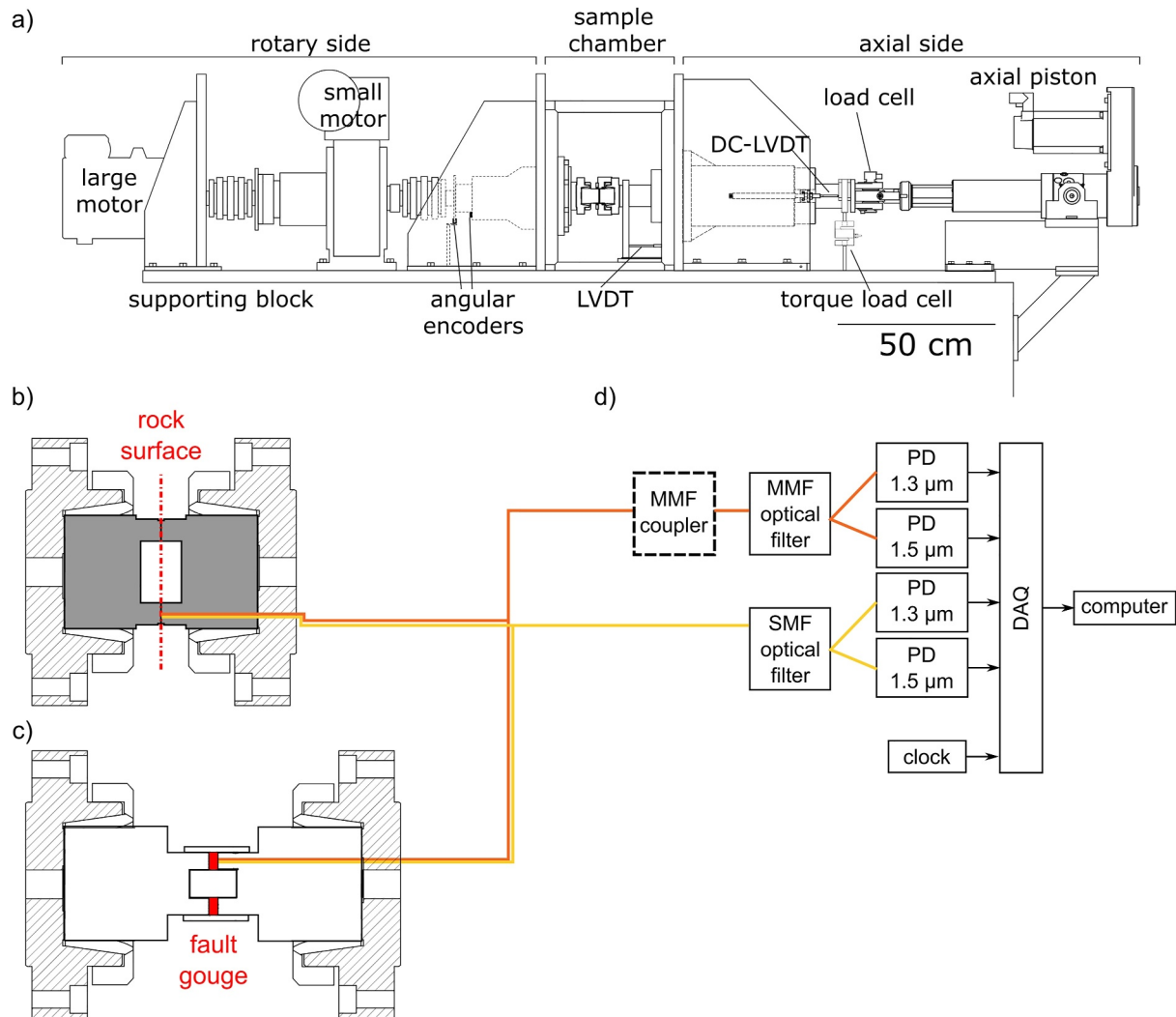
Figure 1. Experimental setup. (a) SHIVA apparatus. Cross section of the sample chamber: (b) sample holder setup for bare-rock high velocity friction experiments (HVFEs): two hollow cylinder rock samples are indicated in gray, (c) sample holder setup for gouge HVFEs. (d) The two-color pyrometer measurement setup connected to the fibers collecting infrared radiation from the bare-rock sample surface or gouge layer boundary.

that will be in contact with the gouge layer. Teflon rings were fixed with screws to the rotary half of the sample assembly to impose strain localization at the boundary between the gouge layer and the sample holder attached to the stationary side (Cornelio et al., 2024; Rempe et al., 2017). Teflon rings were tightened with a hose clamp to have lateral confinement of the gouge layer during the experiment. The gouge layer, composed of 3 g of Carrara marble powder, had an initial thickness of ~3 mm and was sandwiched between the two halves of the sample assembly (Figure 1c).

SHIVA acquisition system recorded at 4–12,500 Hz the measurements of normal force and torque from two load cells, axial displacement from a high-resolution LVDT, incremental rotation from two digital encoders (Figure 1a) and a synchronization signal obtained with a function generator connected to both SHIVA and the two-color pyrometer. Normal and shear stress (τ) were calculated from the normal force and torque (Tsutsumi & Shimamoto, 1997). Slip (δ) and slip rate (V) were calculated from the incremental rotation as the tangential slip and slip rate values referred to an equivalent radius which coincided with the radial positioning of the two fibers. Shortening, defined as the displacement normal to the shearing surface or gouge layer was calculated from the axial displacement, zeroed at the onset of slip. Each bare-rock HVFE (Table S1 in Supporting Information S1) consisted in gradual increase of the normal stress up to 20 MPa, followed by shear deformation imposing a boxcar slip rate function with equal acceleration and deceleration of 6.4 m/s^2, a target slip rate of 6 m/s and a total

displacement of 20 m. We performed the gouge HVFEs (Table S2 in Supporting Information S1) at a normal stress of 20 MPa (except s1863 and s1865, at 30 MPa), with either a boxcar slip rate function with acceleration and deceleration ramps of 6.4 m/s², target slip rate of 1 m/s, and slip of 1 m or a regularized Yoffe slip rate function (Tinti et al., 2005) with rise time of 2 s, smoothing time of 0.1 s and total slip of 1.65 m, following the procedure in Harbord et al. (2021).

2.2. Two-Color Pyrometer

The pyrometer setup we used was the updated version of one used in previous studies (Aretusini, Núñez-Cascajero et al., 2021; A. Núñez-Cascajero et al., 2020; Tapetado et al., 2016). Here, we used a singlemode fiber (SMF) together with a multimode fiber (MMF) (Figure 1b). The SMF fiber, with core and cladding diameter of 9 and 125 μm and numerical aperture of 0.14, was connected to an optical filter (low insertion loss wavelength selective filter) splitting the radiation into two bands centered at 1.31 and 1.55 μm, respectively, and to low noise photoreceivers (InGaAs photodetectors and transimpedance amplifiers), to convert the radiant flux into a voltage signal (Tapetado et al., 2016). The MMF fiber, with core and cladding diameter of 62.5 and 125 μm and numerical aperture of 0.275, was connected to an optical coupler in some cases (i.e., in bare-rock HVFEs and not in gouge HVFEs), to an optical filter and then to a low-noise photodetector. Before each acquisition, the gain of the amplifiers was set to low gain for the MMF and high gain for the SMF and the range of the voltage signals in the DAQ input were set to 0–10 V. This was done to avoid that the amplified signal exceeded the dynamic range so that the output signal resulted truncated and therefore unusable. In each experiment we acquired at 1,000 Hz the infrared radiation (radiant flux) in the two bands (1.3 and 1.5 μm) for each fiber (SMF and MMF), for a total of four channels, and, in a fifth channel, a synchronization signal from the same function generator acquired during the HVFE by SHIVA acquisition system.

The pyrometer calibration was done with a Pegasus 1,200°C dry-block calibrator equipped with a blackbody source. Both optical fibers have been used to calibrate the system for the configuration described above. The optical fibers were positioned 3 mm away from the blackbody surface, they were positioned with a pyramid of needles and pasted with the high temperature glue (Everbuild). Then the temperature was risen from 150 to 1,100°C in steps of 25°C. In this way, the relation between the output voltage proportional to the radiant flux I_D (V) and temperature T (°C) was defined. The radiant fluxes measured during the HVFEs, $I_{D,1.3}$ and $I_{D,1.5}$, corresponding to the two spectral bands centered at 1.31 and 1.55 μm, after the data acquisition card (DAQ) were converted to single channel temperatures $T_{1.3}$ and $T_{1.5}$ using the relation obtained in the calibration tests and assuming that the surface emissivity was the same both in the calibrator and during the experiment (i.e., $\varepsilon_c/\varepsilon = 1$).

2.3. Data Reduction

The synchronization waveform produced with a function generator was acquired up to 12,500 Hz from SHIVA acquisition system and at 1,000 Hz with the pyrometer acquisition system. During post processing of the data, we synchronized the SHIVA and pyrometer time series by matching the clock signals, introducing a time correction to the pyrometer data. Then, to plot the temperature measurements against the measured quantities of SHIVA data acquisition system, the pyrometer data was linearly interpolated by means of the synchronized pyrometer time recording to SHIVA time recording.

2.4. Numerical Models

The evolution of temperature T with time t in the direction z normal to the fault plane (1D model) was defined by the general partial differential equation of heat conduction (Cornelio et al., 2022; Nielsen et al., 2021, and references therein):

$$\rho c \frac{\partial T}{\partial t} = k \frac{\partial^2 T}{\partial z^2} + S(t) \tag{1}$$

with density ρ, heat capacity c, and $S(t) = S_{so}(t) + S_{si}(t)$ the sum of all the volumetric heat sources $S_{so}(t)$ and sinks $S_{si}(t)$ (W/m³). The heat source S_{so} included the frictional heating term, that was calculated as Nielsen et al. (2021):

$$S_{so}(t) = \beta \cdot \tau(t) \cdot V(t) \cdot \delta_{reg}(z) \tag{2}$$

with β the Taylor-Quinney coefficient (Taylor & Quinney, 1934) which represents the fraction of mechanical work rate converted into heat. In our case, β was set to 1, shear stress $\tau(t)$ and slip rate $V(t)$ were both measured directly during the experiments. $\delta_{\text{reg}}(z)$ is a regularized Dirac delta that represents the evolution of strain rate in space (Schiano Di Cola et al., 2021):

$$\delta_{\text{reg}}(z) = \frac{1}{4\gamma} \cdot \cos\left(\frac{\pi z}{2\gamma} + 1\right) \tag{3}$$

With z the direction orthogonal to the contact/sliding surface, γ the regularization parameter, set to $0.5 \cdot dz$ (with model step dz ranging here from 1 to 5 μm). Strain rate is the product of $\delta_{\text{reg}}(z)$ and $V(t)$.

In the definition of S_{so}, it was typically assumed that: (a) the product between shear stress and slip rate, namely the frictional work per unit area per unit time (frictional power density) was fully converted into frictional heat being the heat source (Carslaw & Jaeger, 1959), that is, $\beta = 1$ all mechanical work rate was dissipated as heat (Taylor & Quinney, 1934); (b) the shear stress $\tau(t)$ is an average shear stress across the shearing surface, that is, that the real area of contact/nominal area = 1, and (c) the shear stress $\tau(t)$ and slip rate $V(t)$ were referred to the equivalent radius (i.e., of 20.4 and 11.5 mm in bare-rock and gouge HVFEs, respectively) to simplify the axisymmetric setup of the experiments in which slip rate depended on the sample radius.

The volumetric heat sink S_{si} was calculated as the energy consumed during calcite decomposition via decarbonation reaction (Sulem & Famin, 2009):

$$S_{\text{si}}(t) = X_{\text{CaCO}_3} \cdot (1 - \varphi) \cdot \rho \cdot \frac{\Delta H}{MM_{\text{CaCO}_3}} \cdot \frac{\partial \xi}{\partial t} \tag{4}$$

with X_{CaCO_3} the fraction of calcite contained in the material set equal to 1, φ the porosity (5% and 15% in bare-rock and gouge HVFEs, respectively), ΔH the reaction enthalpy (−177.8 kJ/mol), MM_{CaCO_3} the molar mass of calcite (0.1 kg/mol), and $\partial \xi / \partial t$ the reaction rate (1/s) (Sulem & Famin, 2009). The ratio $\Delta H / MM_{\text{CaCO}_3}$ was the latent heat of decarbonation reaction (kJ/kg) and the negative sign of reaction enthalpy represented the endothermic decarbonation reaction acting as a heat sink. For calculating the reaction rate we assumed that decarbonation follows a first order reaction kinetics (Rodriguez-Navarro et al., 2012):

$$\frac{\partial \xi}{\partial t} = \text{Arh}(T) \cdot \exp(-t \cdot \text{Arh}(T)) \tag{5}$$

with $\text{Arh}(T)$ the Arrhenius function described as:

$$\text{Arh}(T) = A \cdot \exp\left(-\frac{E_A}{R \cdot T}\right) \tag{6}$$

with A the pre-exponential factor (3.82×10^7 1/s), E_A the activation energy (179.9 kJ/mol) (Rodriguez-Navarro et al., 2009), R the Boltzmann's constant (8.314×10^{-3} kJ/(mol · K)), and T the temperature (K).

For bare-rock HVFEs, the model was set as 1D, with z direction orthogonal to the contact/sliding surface, which was in $z = 0$ (Figure 2a). The space domain was in the range $z = \pm 0.10005$ m and was discretized into 50,053 nodes ($dz = 4 \times 10^{-6}$ m) whereas the time domain (5 s) was divided into 1,001 nodes ($dt = 0.005$ s). The space domain had thermal properties of Carrara marble rocks (Table S3 in Supporting Information S1). For gouge HVFEs, the model was also set as 1D, with z direction orthogonal to the fault gouge layer (Figure 2b). The space domain was organized in three subdomains: (a) downstream forcing block, (b) gouge layer, and (c) upstream forcing block. The thickness of (a) and (c) was set to 0.1 m and had the thermal properties of the metal alloy composing the sample holder, whereas (b) had the thermal properties of Carrara marble gouge (Table S3 in Supporting Information S1). The thickness of subdomain (b) depended on the gouge thickness w during the experiments (generally below 3 mm due to gouge compaction). The center of the heat source was positioned in $z = 0$ ("Mid" in Figure 2b), the position of the boundary between subdomain 2 and 3 ("Us" in Figure 2b) was set a distance $w_0 = 2 \times 10^{-4}$ m from the heat source. The position of the boundary between subdomain 1 and 2 was set
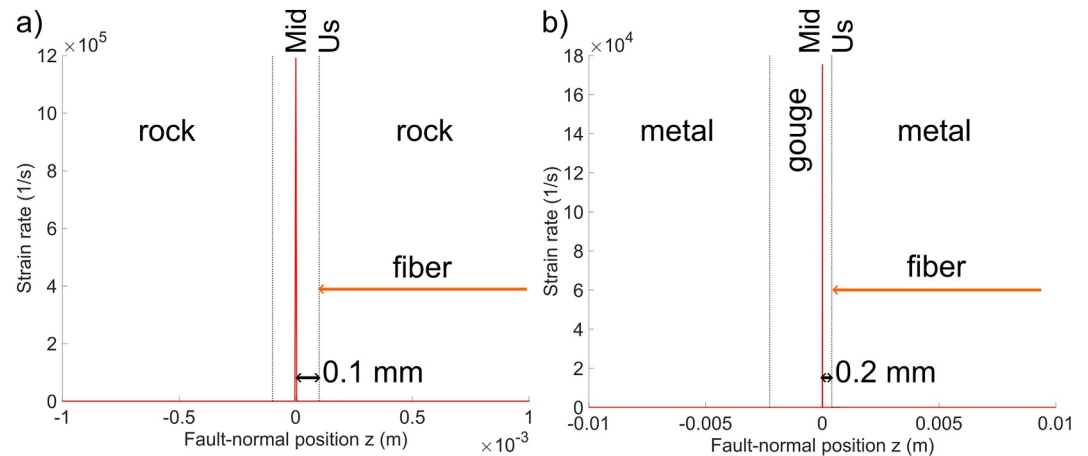
Figure 2. Numerical modeling setup. The $\delta_{\text{reg}}(z)$ strain rate function across the fault normal position. (a) bare-rock and (b) gouge high velocity friction experiments (HVFEs). The maximum degree of localization occurred always in $z = 0$ m, where temperature T_{Mid} was calculated. T_{Us} was calculated 0.1 mm away from T_{Mid} in bare-rock HVFEs, depending on the uncertainty of the fiber tip positioning or 0.2 mm away in gouge HVFEs due to the relative distance between the localized zone and the fiber tip positioning. T_{Us} was then compared with the measured temperature (Figures 3 and 4).

at a distance $w - w_0$. The strong asymmetry in the position of the heat source within the gouge layer was motivated by microstructural observations that place the principal slipping zone at about 2×10^{-4} m from the gouge and stationary sample holder boundary (Demurtas et al., 2021; Pozzi et al., 2018; Rempe et al., 2017; Smith et al., 2015). This distance was the one where the measuring tips of the fibers are placed, considering the roughness of the sample holder. The space domain was discretized into a variable number of nodes so that $dz \sim 10^{-5}$ m and the time domain (i.e., 2.5 s for the boxcar or 3.5 s for the Yoffe slip rate functions, respectively) was divided into 1,001 nodes ($dt = 2.5$–3.5×10^{-3} s). At the first and last node, a constant temperature was set to 298 K (25°C) (i.e., Dirichelet boundary condition). The initial temperature in all model nodes was 298 K. The heat sources and sinks were set in all model nodes for bare-rock HVFEs and only in subdomain (2) for gouge HVFEs. The model solved Equation 1 using the finite difference implicit backward time, centered space method (Aretusini, Meneghini, et al., 2021; Gerya, 2019). After each simulation, temperature $T_{\text{m,Mid}}$ was referred to the node coincident with the maximum of the strain rate function $\delta_{\text{reg}}(z)$, always in $z = 0$ m, and temperature $T_{\text{m,Us}}$ was referred to the node in $z = 10^{-4}$ m in bare-rock HVFE (Figure 2) and to the boundary node between subdomains 2 and 3 at $z = 2 \times 10^{-4}$ m in gouge HVFE. These positions coincide with the position of the optical fiber tip during the experiments, which will be compared with the measured temperatures.

3. Results

3.1. Thermo-Mechanical Behavior and Thermal Modeling

In all HVFEs (Figures 3 and 4) the temperatures were measurable from the two fibers pyrometer system when higher than ∼400°C, as shown in our previous work (Aretusini, Núñez-Cascajero et al., 2021). We compared the modeled temperatures $T_{\text{m,Mid}}$ and $T_{\text{m,Us}}$ with the measured temperature $T_{1.5}$ of the SMF (Figure 3b for bare-rock, Figures 4b and 4d for gouge). Hereafter we discuss the comparison between the modeled temperature and $T_{1.5}$ since both SMF and MMF fibers were similar (Figures 3b, 4b, and 4d). Temperature $T_{1.5}$ was spatially equivalent to $T_{\text{m,Us}}$ in both gouge and bare-rock HVFEs, assuming a reasonable spatial positioning uncertainty of ca 1–2×10^{-4} m, whereas $T_{\text{m,Mid}}$ was the maximum expected temperature. To facilitate the interpretation of results we identify different stages in the evolution of friction, that is, the ratio between shear stress and normal stresses, and temperature with slip.

3.1.1. Bare-Rock HVFEs

In bare-rock HVFEs we recognized four stages (i–iv) characterizing the evolution of friction as a function of slip (Figure 3). Friction is here defined as the ratio between the shear stress and the normal stress. These stages are therefore used to interpret temperature evolution with slip. The "Initial" stage (i) is the one in which friction
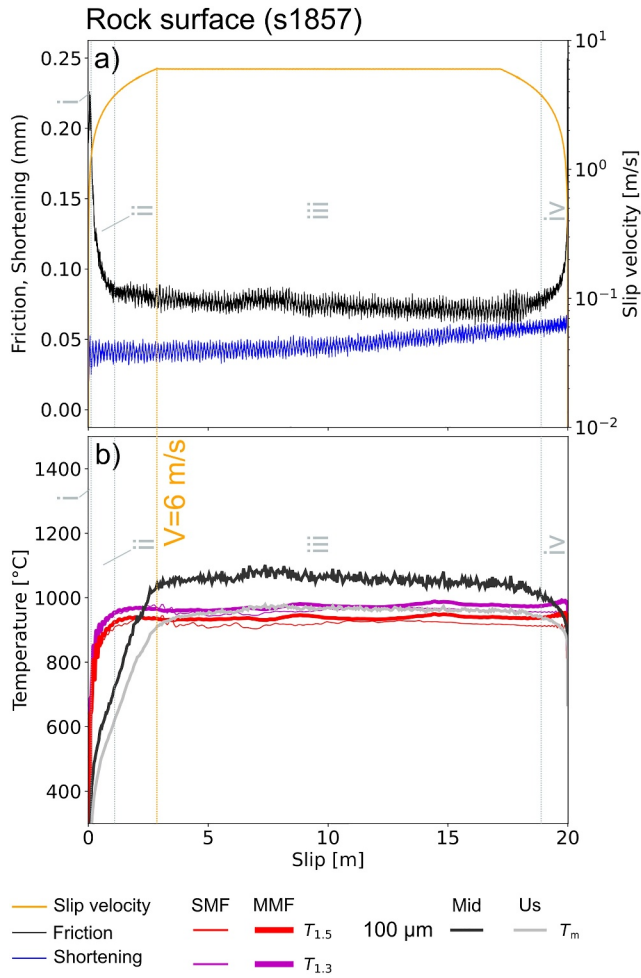
Figure 3. Results for bare-rock high velocity friction experiment s1857 performed at normal stress of 20 MPa. (a) Measured friction (computed as the shear to normal stress ratio) and sample shortening (thickness changes) compared with imposed slip rate as a function of slip. (b) Comparison between measured ($T_{1.5}$ and $T_{1.3}$) and modeled temperature at the center (T_{Mid}) and at the measuring boundary (T_{Us}) versus slip. Four stages are identified (see main text). The vertical orange line indicates the value of slip at which slip rate achieves the plateau at 6 m/s.

reached the peak value of 0.65, achieved after 0.007 m of slip (0.06 s), when slip rate increased from 0 to 0.4 m/s, with no measurable temperature. This was followed by (ii) the "dynamic weakening" stage characterized by a fast decrease of friction from 0.7 to 0.08, completed at 1.8 m of slip (0.75 s) with slip rate accelerating from 0.4 to of 5 m/s. Temperature increased from 400 to 900–1,000°C. Therefore, we observed a (iii) so-called "Dynamic sliding" stage with nearly constant friction (slowly decreasing from 0.08 to 0.05) maintained up to 17.15 m of slip, with constant temperature of 950°C and constant slip rate of 6 m/s. This stage was interpreted as the sliding at the dynamic friction level (nearly constant). The (iv) "Final" stage with friction increasing to its final value was associated with slip deceleration imposed by the experiment. Before final arrest, when the slip rate decreased in the deceleration ramp, friction increased to a maximum of 0.25 at 19.8 m of slip for a slip rate of ∽2 m/s and measured temperature slightly decreased from 950 to 925°C.

During the experiment, shortening was almost negligible and occurs mostly in stage (i), when the friction reaches its peak value. Due to sample misalignment during installation of samples in SHIVA sample chamber, the peak friction values in stage (i) were quite scattered across the experiments presented here. Such variability impeded us to distinguish the effect of the imposed initial roughness on the temperature increase (Figure S1a in Supporting Information S1).

In bare-rock HVFEs, modeled $T_{m,Us}$ was referred to $z \sim 10^{-4}$ m (Figure 3b). In stage (ii), modeled $T_{m,Us}$ increased at a lower rate than measured $T_{1.5}$ and it was lower than $T_{1.5}$ at the transition to stage (iii). Then, in stage (iii), $T_{m,Us}$ reached and slightly exceeded $T_{1.5}$ after ∽2.5 m of slip, which corresponded to the end of the acceleration ramp of the boxcar slip rate function (i.e., when slip rate became constant at 6 m/s). Noteworthy, between 1.8 and 2.5 m of slip, though the imposed slip rate increased from 3 to 6 m/s, the dynamic friction and the measured temperature $T_{1.5}$ were constant (∽0.05 and 925–950°C, respectively). Instead, in the same slip range, the modeled temperature $T_{m,Us}$ increased and eventually matched the measured $T_{1.5}$ only after 2.5 m of slip when the imposed slip rate was constant. In stage (iv), $T_{m,Us}$ decreased faster than $T_{1.5}$, also after the sample stopped and was cooling down (Figure S2 in Supporting Information S1).

3.1.2. Gouge HVFEs

In gouge HVFEs performed by imposing the boxcar slip rate function (Figures 4a and 4b), we also recognized four stages analog to those in bare-rock HVFEs. (i) The "initial" stage with friction coefficient increasing up to 0.7, achieved at ∽0.002 m (0.03 s), with slip rate increasing from 0 to 0.14 m/s and no measurable temperature. This stage was followed by a slip hardening substage with friction increasing from 0.7 to 0.8, achieved at 0.044 m of slip (0.11 s), with slip rate increasing from 0.14 to 0.72 m/s and no measurable temperature. The "dynamic weakening" stage (ii) was characterized by a sudden decrease of friction from 0.8 to 0.4, achieved at 0.07 m (0.14 s), with slip rate of 1 m/s and no measurable temperature. Therefore, (iii) in the "dynamic sliding" stage friction decreased gradually from 0.4 to 0.25, which is achieved at 0.88 m (1 s), when slip rate was constant (1 m/s) and temperature is in the 550–600°C range. The "final" stage (iv) was characterized by increasing friction coefficient up to a peak value of 0.4 achieved at 0.93 m (1.14 s), when slip rate decreases from 1 to ca 0.08 m/s, and temperature remains in the 550–600°C range.

In gouge HVFEs performed by imposing the regularized Yoffe slip rate function (Figures 4c and 4d), we used the same four stages to interpret our results. In the "initial" stage (i) friction increased up to 0.7 at ca 0.001 m (0.01 s), with slip rate increasing from 0 to 0.2 m/s and no measurable temperature. This stage was followed by a substage
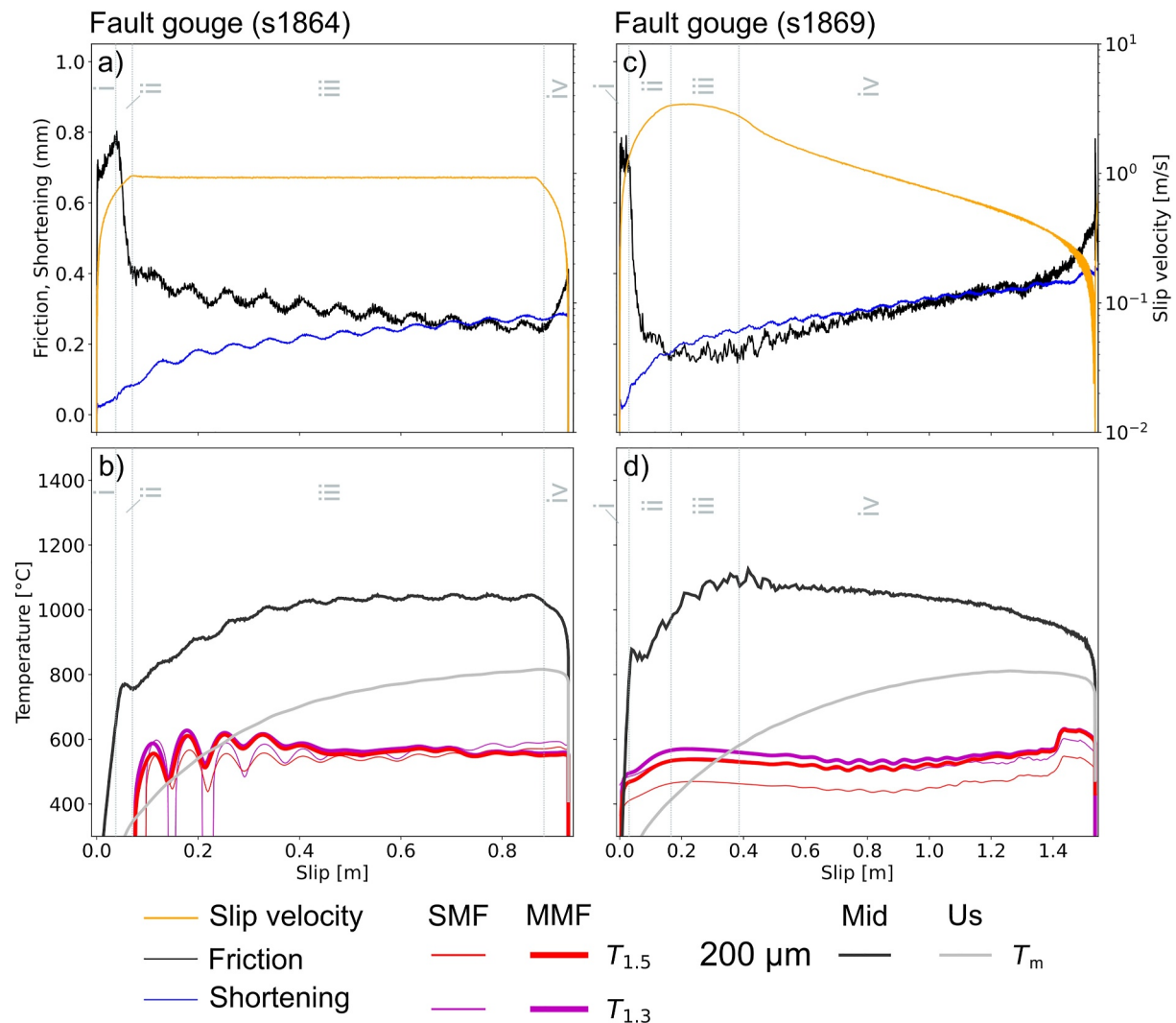
Figure 4. Measured friction (=Shear stress/normal stress) and temperature, modeled temperature at center (T_{Mid}) and at measuring boundary (T_{Us}) vs. slip. Two gouge high velocity friction experiments were both run at 20 MPa normal stress, with: (a) and (b) boxcar slip rate function (s1864), (c) and (d) regularized Yoffe slip rate function (s1869). The recognized four stages (i) to (iv) are indicated.

with nearly constant friction with slip (friction remains equal to 0.7) up to 0.03 m (0.06 s), with slip rate increasing from 0.2 to 1.4 m/s, and temperature becoming measurable toward the end of the stage with values of 500–550°C. The "dynamic weakening" stage (ii) was characterized by an initially fast and then slower decrease of friction from 0.7 to 0.2 at ~0.18 m (0.11 s), with slip rate accelerating to its peak value of 3.5 m/s, and temperature increasing to 550–600°C. During the (iii) "dynamic sliding" stage imposed slip rate was slowly decreasing from 3.5 to 2.0 m/s, the friction coefficient was nearly constant ranging between ~0.2 and 0.18 at 0.4 m of slip and temperature being constant in the 550–600°C range. The "final" stage (iv) was characterized by an increasing friction coefficient from ~0.2 at 0.4 m to 0.53 at 1.54 m (2.15 s) of slip, with slip rate decreasing from 2 m/s to 0 m/s and temperature being constant in the 550–600°C range. In all gouge HVFEs, about 2/3 of total shortening occurred in the initial stages (a) and (b) until the achievement of dynamic weakening was completed. Then, the remaining 1/3 of shortening occurred gradually until the end of slip in stages (iii) and (iv).

In gouge HVFEs temperature models, $T_{m,Us}$ was referred at $z \sim 0.2 \times 10^{-4}$ m and the maximum $T_{m,Us}$ (1,100–1,000°C) was about twice the measured one $T_{1.5}$ (500–550°C) (Figures 4b and 4d). Moreover, the gouge HVFEs confirmed that the measured temperature $T_{1.5}$ remained constant during the stage following initial dynamic weakening, and independently of the imposed slip rate function (boxcar or regularized Yoffe). As was the case for

the bare-rock HVFEs (Figures 3a and 3b), also for gouges, the maximum modeled temperatures $T_{m,Us}$ were higher than the measured ones $T_{1.5}$ (see also Figure S3 in Supporting Information S1).

4. Discussion

The temperature measurements presented in this study are unique because collected very close to the bare-rock sliding/contact surface (see also Aretusini, Núñez-Cascajero et al., 2021) or to the gouge layer "Us" boundary, situated between the gouge layer and the sample holder attached to the axial side of SHIVA apparatus (Figure 2). In fact, previous studies used pyrometers, thermocouples or infrared cameras to measure temperature far or outside the slip zone during simulated seismic slip, likely resulting in underestimation of temperature due to sample cooling during the experiment (Han et al., 2007; Noda et al., 2011). Moreover, our measurements were performed at high acquisition rate (1,000 Hz) and did not require to wait for the characteristic time interval (0.1–1 s) that thermocouples would require, allowing for the tracking of temperature during dynamic weakening. Although further work is needed to improve the temperature measurements and extend them to different fault materials and loading conditions, in the following we discuss our experimental results to emphasize several key features regarding the role of temperature in dynamic weakening and the contribution of dissipative processes in the earthquake energy budget in calcite-bearing faults.

4.1. Temperature Evolution During Experiments

The first feature emerging from our experiments was the constant measured temperature $T_{plateau}$ at high slip values (>1 m in bare-rock, and >0.2 m in gouge HVFEs) observed during dynamic sliding stage (iii) (Figures 3 and 4). In fact, despite increasing slip should correspond to frictional heating and temperature increase in the slip zone, the temperature remained constant ($T_{plateau}$) in both bare-rock and gouge HVFEs at ~950°C and ~500–600°C, respectively (Figures 3 and 4). Temperature remains constant also during the deceleration stage (iv), which is a relevant part of the friction evolution for the imposed Yoffe function (Figures 4c and 4d). Moreover, temperature was nearly constant also in most of the dynamic weakening (stage ii); this is more evident for bare-rock surfaces (Figure 3). In the case of gouge HVFEs, temperature was constant independently of the imposed slip rate function (boxcar or Yoffe) (Figure 4). These observations confirm the presence of an energy sink, identified as the latent heat caused by calcite decarbonation, affecting the energy budget. It appeared that the value of the constant temperature depends on the imposed slip rate, rather than on the evolution of the slip rate with slip. Indeed, a constant temperature of ~950°C is reached for a slip rate of 6 m/s (Figure 3b), while a temperature of ~600°C was measured for a constant slip rate of 1 m/s (Figure 4b). For the imposed Yoffe function (Figure 4d), the constant temperature was slightly less than the one resulting from the application of the boxcar slip rate function, despite the peak slip rate was larger (3.5 m/s) but rapidly decreasing. This might suggest that the achievement of a constant temperature value did not depend on the maximum slip rate but on its average value over the entire duration of the experiment.

The second striking feature, resulting from the comparison with the modeled temperatures $T_{m,Us}$ or the measured ones from previous studies (Han et al., 2007), was the extremely rapid increase of the measured temperature $T_{1.5}$ during the dynamic weakening stage (ii) in our bare-rock (Figure 3b) and gouge with Yoffe slip rate function (Figure 4d) HVFEs. In general, at the beginning of stage (ii) the dynamic weakening was possibly associated with flash temperatures developing at asperity (bare-rocks) or grain contacts (gouge), resulting in the "flash heating" process (Beeler et al., 2008; Cornelio et al., 2022; Goldsby & Tullis, 2011; Rice, 2006). Flash heating was proposed to be active in both bare-rocks (Goldsby & Tullis, 2011) and gouges HVFEs (Yao et al., 2018). In all our HVFEs, flash temperatures of individual asperities were probably not measurable with our current experimental configuration because of spatial averaging issues. In fact, flash temperatures of individual asperities were possibly averaged down to a measured temperature below 400°C in the area whose emitted infrared radiation were sampled by the optical fibers (Aretusini, Núñez-Cascajero et al., 2021), corresponding to our minimum measurable temperature. Moreover, the time duration of the flash temperatures is probably too short to be detected with our current acquisition system. The latter operates at 1,000 Hz: if the slip rate is 1 m/s and the asperity size 1–10 μm (Dieterich & Kilgore, 1994), the duration of the sliding contacts and of the associated flash temperature will last 1–10 μs, so well below the current acquisition rate of 1,000 Hz.
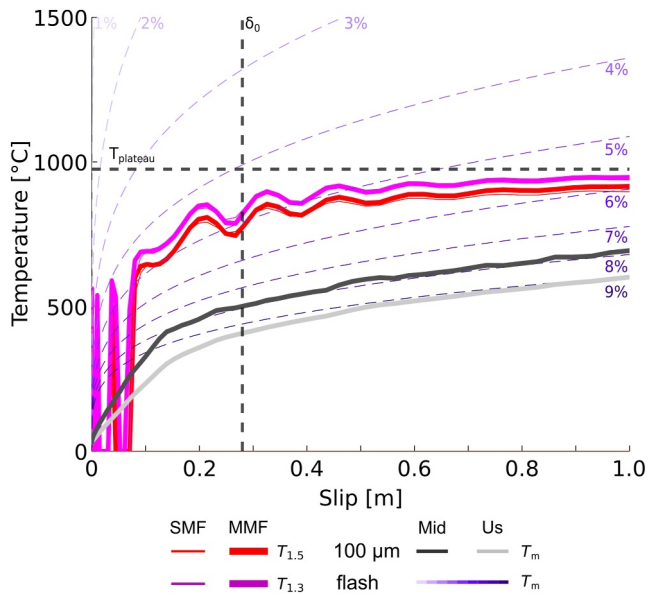
Figure 5. Comparison between measured temperatures (red and purple lines), modeled bulk temperatures (light and dark gray lines) and asperity-scale flash temperatures (violet dashed lines) for bare-rock high velocity friction experiment (HVFE) s1857 during the first meter of slip. Asperity-scale flash temperatures were computed using different ratios of real contact area to total area (Ar/A) ranging between 1% and 9%. The temperature plateau ($T_{plateau}$) indicates the constant temperature measured for bare-rock HVFEs. δ_0 indicates the slip switch value denoting the transition between asperity-scale and bulk scale processes (Cornelio et al., 2022).

To further investigate this point, we have compared for bare-rock HVFEs our measured temperatures with the modeled bulk and flash temperatures, for slip <1 m, during stage (ii) (Figure 5). Flash temperatures were calculated as Cornelio et al. (2022), Rice (2006):

$$T_{flash} = \left(\rho c \sqrt{\pi \frac{k}{\rho c}} \right)^{-1} \tau_p \frac{A}{A_r} V(t) \sqrt{\frac{D}{V(t)}} \qquad (7)$$

With ρ, c, and k the density, heat capacity and thermal conductivity of carrara marble (Section 2.4), τ_p the peak shear stress (ca. 13 MPa), A the sample contact area (0.0013 m^2), A_r the real area of contact, $V(t)$ the slip rate evolution during the HVFE and D the size of one asperity (68 μm), numerically optimized (Cornelio et al., 2022). T_{flash} was calculated for Ar/A ratios from 1% to 9%. Modeled bulk temperatures were lower than measured ones, and were comparable to flash temperatures when the Ar/A ratio was high (8%–9%) and only for slip higher than δ_0, the slip-switch distance at which the bulk rather than the asperity-scale frictional processes start to control the shear stress evolution (Cornelio et al., 2022). Measured temperatures were higher than modeled ones and they were comparable to flash temperatures only for low values of the Ar/A ratio (4%–5%) and for slip values lower than δ_0. This suggests that the measured temperature increase was likely caused by flash temperatures of a group of asperities around the measurement location (Figure 3b), which were realistically smaller than the flash temperature of a single asperity (Dieterich & Kilgore, 1994) (approximated by flash temperatures for $Ar/A \sim 1\%$) but larger than the bulk temperature (Cornelio et al., 2022). With increasing slip, the measured temperature became nearly constant, approaching $T_{plateau}$, likely because of the combination of Ar/A ratio increase and heat sink activity at the scale of a group of asperities (Figure 5). Future work will be aimed at quantifying the increase in contact area by surface roughness analysis to assess the importance of contact area saturation in buffering temperature. Finally, at larger slip values (>2.5 m), the measured temperature and the modeled bulk temperature for bare-rock surfaces become similar (Figure 3). The occurrence of extreme heating at the asperity scale due to stress concentration and seismic slip rates (Cornelio et al., 2022; Nielsen et al., 2021) can induce a variety of deformation processes in carbonate rocks such as dislocation avalanches, calcite thermal decomposition and deposition of amorphous carbon (Spagnuolo et al., 2015).

For comparison, in our gouge with boxcar slip rate function HVFEs, neither flash temperatures nor group of grain contacts temperatures were detectable during stage (ii), likely because strain was not yet localized in a principal slip zone (PSZ) close to the boundary where the fiber was installed (Figure 4b), as indicated by the occurrence of slip strengthening behavior during stage (a) (Pozzi et al., 2018; Rempe et al., 2017; Smith et al., 2015). In our gouge with boxcar and Yoffe HVFEs, we performed additional temperature models in which the effect of evolving porosity due to compaction and strain localization was tested (Figure S5 in Supporting Information S1). Thermal properties and heat sinks were modeled with constant porosities of 5%, 10%, 15%, 20%, 25%, 30%, 35%, and 40% in individual numerical models. We observed the lowest difference between modeled and measured temperatures during stages (i) and (ii) when considering the highest porosity value (40%) which promoted the highest temperatures. However, the difference between modeled and measured temperatures increased during stages (iii) and (iv) even when considering the lowest porosity value (5%) which promoted the lowest temperatures.

A third notable feature was the mismatch between modeled and measured temperatures during the stages (iii) and (iv) characterized by relatively constant friction coefficient followed by slip deceleration and arrest. In the case of sheared gouges, the modeled temperature was about twice the measured one (1,100°C vs. 550°C, Figures 4b and 4d). In the case of sheared bare bare-rock surfaces was 15% higher (1,100°C vs. 950°C, Figure 3b) and the modeled and measured temperatures overlapped only when the measuring point was located at ~0.1 mm from the sliding surface (T_{Us} in Figure 3b). The modeled temperatures included the energy sink due to decarbonation (see

below). The evolution of modeled temperature during the initial dynamic weakening and the following stages was controlled by the imposed slip rate function. This is expected because the heat source depends on slip rate ($\propto \tau \times V$). Furthermore, it is quite evident the difference between the two modeled temperatures (T_{Us} and T_{Mid}), which is larger for the gouge HVFEs. This is due to the different position of measurement points used for computing temperatures and the extreme temperature gradient occurring during the experiments in the direction orthogonal to the experimental fault. The mismatch between modeled and measured temperatures observed for gouge HVFEs questioned the adopted theoretical formulation and will be discussed below.

A fourth feature are the measured low cooling rates, compared to those predicted by the models, once the sample stopped at the end of the slip (Figures S2 and S3 in Supporting Information S1). Since the samples with their slip zones are collected after the experiments to perform microstructural investigations aimed at identifying the deformation mechanisms operating during simulated seismic slip (Demurtas, Smith, Prior, Brenker, & Di Toro, 2019; Pozzi et al., 2019), low cooling rates may impact on the post-slip microstructural evolution. For instance, sintering processes are controlled by diffusive processes promoted by the value (500–700°C) and duration of the temperature imposed to calcite aggregates (Covey-Crump, 1997). As a consequence, the original microstructures associated with coseismic slip might be overprinted during cooling and the deformation mechanism associated with coseismic slip not directly recognizable.

4.2. Microstructures and Deformation Processes

We discuss here the deformation processes that promoted dynamic weakening during our experiments at seismic slip rates by interpreting scanning electron microscope back scattered electron (SEM-BSE) and secondary electron (SEM-SE) images (Figure 6) (Aretusini, Núñez-Cascajero et al., 2021; Cornelio et al., 2024). After the HVFEs, the samples were recovered, impregnated in epoxy resin and cut tangential to their circumference at the equivalent radius distance (i.e., $r \sim 20$ mm in bare-rock and $r \sim 11$ mm in gouge samples) to obtain ultra-polished cross-sections for high-resolution microstructural analysis. Alternatively, bare-rock samples were recovered and the fault surface observed with SEM-SE. Post-mortem bare-rock HVFEs samples had locally the fault surfaces welded (i.e., adhesive welding). Post-mortem gouge HVFEs samples appeared as a compacted powder that was cohesive next to the fault slip surface, located at the contact between the gouge layer and the stationary sample holder (Cornelio et al., 2024).

In bare-rock HVFEs, we discuss microstructures obtained during the acceleration toward the target velocity of 6 m/s, but stopped after 1 m of slip displacement, from a cross-section (Figures 6a–6c) and those obtained after the entire experiment (27.7 m of slip) from the sheared rock contact (Figures 6d–6f). In the cross-section, we observed highly porous domains (Figures 6a and 6b), suggesting the occurrence of decarbonation reaction, and low porosity domains (Figure 6c), indicative of high temperature sintering and crystal plastic processes. Decarbonated and sintered microstructures constituted a ca. 50 µm thick band around the contact surface and transitioned to the intact, undeformed rock. In particular, at slip initiation (slip = 1 m), microstructural evidence of decarbonation was coherent with the measured temperature plateau of ~950°C after 1 m slip where imposed slip velocity was 3 m/s (Figure 5). At the end of the experiment (i.e., slip = 27.7 m), the sheared rock contact included an ultra-polished fault surface made by grains with size of ~0.1–5 µm (Figure 6f) with a ca. 50 µm PSZ beneath (Figures 6d and 6e). The interpretation of our microstructural observations is in agreement with those from previous works in which carbonate gouge or bare-rocks were sheared at seismic slip rates in absence of pore fluid under unconfined conditions at low (<40 MPa) stresses (Han et al., 2007). There, microstructural observations documented initial decomposition of calcite into amorphous carbon on the sheared rock contact (Spagnuolo et al., 2015) and, with increasing slip, the development of a <50 µm thick slip zone made of <2 µm in size coatings indicative of grain size dependent viscous creep (Demurtas, Smith, Prior, Brenker, & Di Toro, 2019; Pozzi et al., 2019). Stick-slip experiments in carbonatic bare-rocks, in which seismic slip rate conditions were achieved under confined conditions at higher stresses than ours (50–180 MPa) resulted in microstructural evidence of crystallization from calcite melts (Aubry et al., 2020; Passelègue et al., 2019). A possible explanation for the absence of melt is that unconfined conditions in our bare-rock HVFEs limit the permanence of CO_2 in the slipping zone. The escape of CO, favors the progress of the calcite decarbonation reaction which acts as a thermal buffer, limiting the temperature rise up to the melting point of calcite (Lee et al., 2000).

In gouge HVFEs, we discuss microstructures obtained at the end of the experiment with imposed boxcar slip velocity function. Here, the original grain size of the fault gouge was reduced over a ca. 1,700 µm thick
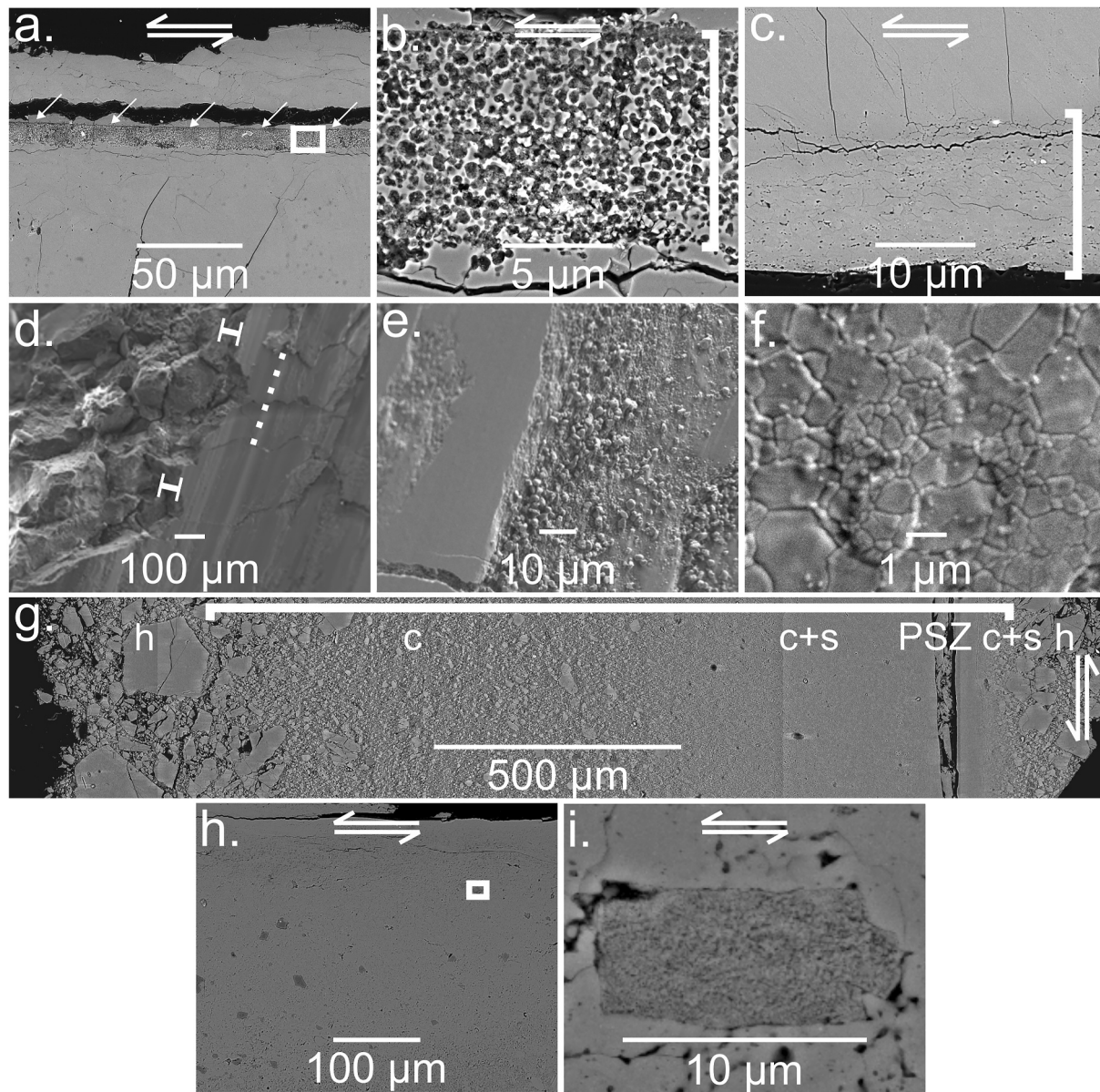
Figure 6. Scanning electron microscope back scattered electron images (SE and BSE) of the sheared rock surface, and of the slip-parallel cross-section, including the slip zone, in bare-rock and gouge high velocity friction experiments (HVFEs). Stationary side of the machine on top. (a–c) Bare-rock HVFE s2007 performed at a normal stress of 20 MPa, slip velocity of 1 m/s, and slip displacement of 1 m (Cornelio et al., 2024). (a) Cross-section of the slip zone (white arrows). The slip zone locally welds the rotary (bottom) and stationary (top) samples; (b) zoom on the highly porous decarbonated layer that developed at expenses of the rotary sample (ca. 10 μm thickness); (c) a ca. 20 μm thick sintered layer formed on the stationary sample. (d–f) Bare-rock HVFE s0086 performed at normal stress of 20 MPa, slip velocity of 6.5 m/s and slip displacement of 27.77 m (Aretusini, Núñez-Cascajero et al., 2021). (d) The slip surface with striations parallel to slip direction (dotted white line). The deforming zone below the slip surfaces can be observed next to a crack edge (white symbols). (e) The smoother areas on the slip surface were coated with (f) polygonal grains (0.1–5 μm grain size). Gouge HVFEs s1960 and s1956 performed at total normal stress of 20 MPa, slip velocity of 1 m/s, total displacement of 1 m (Cornelio et al., 2024). (g) Gouge layer from experiment s1960 (stationary side to the right), cross-section across the deformed gouge layer, with the sequential structure of undeformed gouge (h: host gouge) surrounding microstructural domains (c: comminuted, c + s: comminuted and sintered, principal slip zone (PSZ)) which define a ca. 1,700 μm thick plastic deformation zone (Cornelio et al., 2024). On the right edge, the grooves of the stationary sample holder can be observed, near the position of the optical fibers tip. (h, i) Gouge layer from experiment s1956 (stationary side on top): (h) ca 300–350 μm thick comminuted and sintered domains including few dolomite grains (darker gray clasts). (i) Zoom on a dolomite clast that underwent thermal decomposition, positioned at ca >100 μm from the inferred PSZ. The clast is surrounded by sintered and possibly recrystallized calcite grains (2–5 μm size).

microstructural domain (Figures 6g and 6h). Inside this domain, a PSZ filled with grains with size <0.1 μm (i.e., nanoparticles), could be recognized, bordered by two sharp discontinuities surrounded by low porosity domains containing a matrix of calcite grains with low porosity and few dolomite clasts with a highly porous texture

(Figure 6i). The highly porous grains of dolomite are indicative of decarbonation reactions, similarly as observed in previous experiments performed seismic slip rates (Cornelio et al., 2024; Mitchell et al., 2015). Microstructural observations suggest that dramatic grain size reduction across the gouge layer due to comminution at the onset of slip is progressively overprinted with a PSZ in which strain and heat are effectively localized (Cornelio et al., 2024; De Paola et al., 2015; Demurtas et al., 2021; Pozzi et al., 2018, 2019). In the PSZ, grain size dependent viscous creep, possibly with the contribution of CO_2 pressurization by the calcite decarbonation, was proposed to control the decrease of fault strength (J. Chen et al., 2021; De Paola et al., 2015). In the PSZ surroundings, heat diffusion from the slipping zone was suggested to activate grain sintering and possibly decarbonation reactions. Moreover, in the PSZ surroundings, evidences of distributed plastic strain by comminution in a ca. 500 μm thick domain were related to grain size reduction along calcite crystallographic preferred directions (Demurtas, Smith, Prior, Spagnuolo, & Di Toro, 2019). In the meantime, twinning of calcite was related to distributed plastic strain at similar normal stress (17.5 MPa) but lower velocities (0.01 m/s) than the ones investigated here. At 1 m/s, twinning was negligible therefore plastic strain in the microstructural domains around the PSZ was mainly accommodated by grain size reduction (Demurtas, 2018; Demurtas, Smith, Prior, Spagnuolo, & Di Toro, 2019).

The microstructural observations obtained from our experimentally deformed calcite-bearing rocks under controlled conditions can be reasonably extrapolated to the deformation processes controlling dynamic weakening during seismic slip in natural calcite-rich carbonate rocks such as limestones. In the latter, we expect the decarbonation reaction to occur at higher temperatures as the CO_2 partial pressure increases (Valverde et al., 2015), until decarbonation is preceded by calcite melting (Lee et al., 2000). At the same time, calcite nanoparticles, either produced by the decarbonation reaction, or by extreme comminution, may control dynamic weakening by grain size dependent viscous creep processes (Ashby & Verrall, 1973). Alternatively, nanoparticles could result from recrystallization of carbonatite-like melts (Aubry et al., 2020) and therefore be indirect evidence of fault dynamic weakening by melt lubrication, as occurs in silicate bearing rocks (Nielsen et al., 2008). In any case, the nanoparticle grain size is affected by the post seismic stage, which includes sintering processes, fluid-rock interaction, etc., that lead to grain growth, dissolution, precipitation and eventually to obliteration of the microstructures formed during seismic slip. Therefore, in natural faults in carbonate rocks it is difficult to distinguish microstructures associated with seismic faulting, although highly localized, and nanoparticle-rich PSZs with nanopores likely due to thermal decomposition have been described (Collettini et al., 2013; Demurtas et al., 2016; Fondriest et al., 2015; Niemeijer et al., 2012; Ohl et al., 2020; Rowe et al., 2012; Siman-Tov et al., 2013). Moreover, the experiments discussed here do not include the effect of seismic rupture propagation and dynamic fracturing of wall rocks, often recognized in carbonate-hosted faults (Cortinovis et al., 2024; Demurtas et al., 2016; Fondriest et al., 2015). Dynamic fracturing can lead to a transient increase in permeability in the wall rocks, resulting in the escape of CO_2 from the slipping zone which further promotes the decarbonation reaction. At the same time, experiments showed that dynamic weakening processes are extremely effective, especially in bare-rocks, leading to very low friction coefficient values ($\mu \sim 0.05$) in the initial stages of slip (Spagnuolo et al., 2015), implying that the fault roughness, curvature and structure at the metric scale or higher can largely influence the bulk seismic mechanical behavior of faults (Fondriest et al., 2020; Sagy et al., 2007).

4.3. Energy Sink Due To Decarbonation

The total mechanical work $\mathcal{F}_f$ per unit fault area is given by the area below the shear stress evolution as a function of slip (see Cocco et al., 2023 and references therein):

$$\mathcal{F}_f = \int_0^{t_{tot}} \tau(t)\, V(t)\, dt = \int_0^{\delta_{tot}} \tau(\delta)\, d\delta = W_G + W_{on} + W_{off} \qquad (8)$$

where τ is the on-fault shear stress, V the slip rate, δ the slip. The total mechanical work $\mathcal{F}_f$ is also named frictional work by Cocco et al. (2006, 2023). It is usually partitioned among different dissipation mechanisms: W_G the energy density dissipated to sustain the rupture front propagation (i.e., the fracture energy), W_{on} the energy density dissipated by on-fault processes, and W_{off} the energy density dissipated by off-fault processes (Cocco et al., 2006, 2023 and references therein). In our experiments we do not account for off-fault dissipation, meaning that at first order the contribution of W_{off} can be neglected, also because its significance may arise after dynamic weakening because of thermal cracking (Passelègue et al., 2016). Moreover, we can assume that W_G is small compared to the total mechanical dissipation $\mathcal{F}_f$ and it will likely contribute to earliest stages of the experiment at relatively low
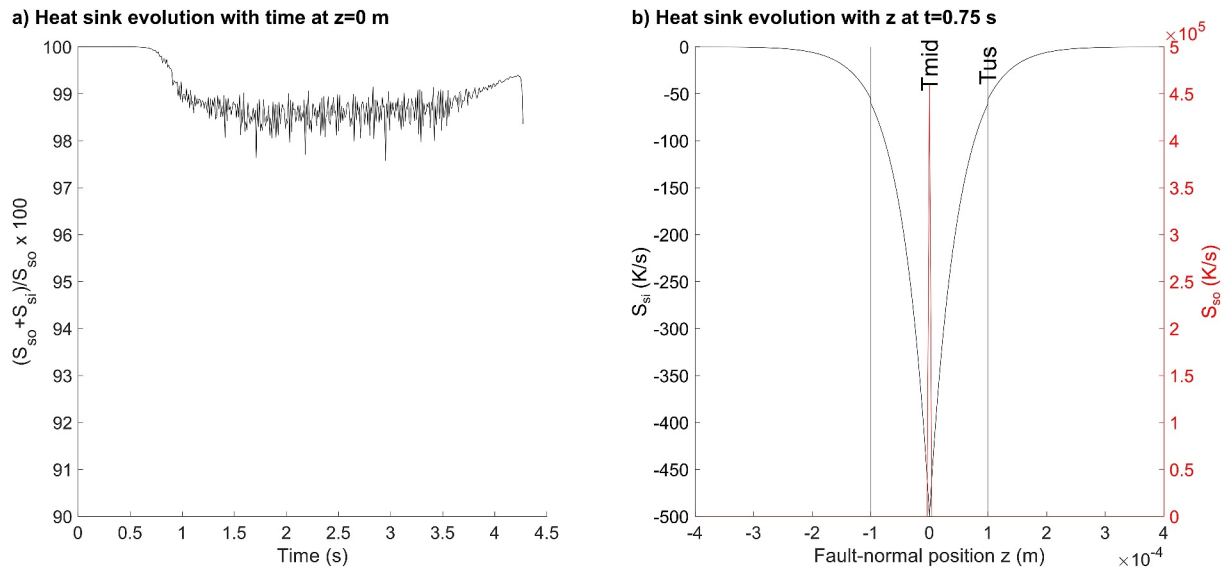
Figure 7. Role of the heat sink, example of a bare-rock high velocity friction experiment (s1684). (a) Evolution of R in $z = 0$ m, shows that up to 2% of heat is absorbed by calcite decarbonation. (b) Evolution of $S = S_{so} + S_{si}$, over the entire model domain (i.e., fault-normal position), at $t = 0.75$ s (dynamic weakening or stage (ii)). S is lower than zero ($S = 0$ is marked by a red dotted line) around the heat source ($\pm 0.25 \times 10^{-3}$ m) because of the endothermic decarbonation reaction.

slip (X. Chen et al., 2021). Therefore, it is likely to assume that we can consider the contribution of W_{on} and in particular how on-fault dissipation contains both the mechanical work dissipated as frictional heat, named S in Equation 1, and the energy dissipated for plastic deformation processes of the on-fault materials, named S_{so} in Equation 2. A common assumption is to consider frictional heat as the only contribution to on-fault energy dissipation (W_{on}) or that the largest portion of $\mathcal{F}_f$ is converted into heat without other energy sinks ($W_{on} = S = S_{so}$ in Equation 2). However, in the case of calcite-bearing rocks, it is necessary to include the endothermic decarbonation reaction (i.e., $CaCO_3$ (s) $\rightarrow$ CaO (s) + CO_2 (g)) as an energy sink because of: (a) the measured CO_2 emission during the experiments and microstructural evidence of calcite decarbonation (Han et al., 2007, 2010; Spagnuolo et al., 2015; Violay et al., 2015), and (b) the results from numerical models which showed the role of this reaction in limiting the temperature increase in the slip zone and in releasing CO_2 which could lead to further weakening by thermochemical pressurization (Goren et al., 2010; Nielsen et al., 2021; Sulem & Famin, 2009). In our temperature models, for endothermic reactions such as decarbonation, heat of reaction S_{si} is negative (Equation 4, Figure 7) and it reduces the mechanical work converted into heat $W_{on} = S_{so} + S_{si}$. This can be investigated by comparing modeled temperatures with and without heat sink. Indeed, the measured temperature is closer to the modeled temperature including heat sinks by decarbonation reactions (Figures 3b, 4b, and 4d and Figure S4 in Supporting Information S1) rather than the one without them. To determine if there is a contribution of the heat sinks to the energy budget, we introduce (Figure 7):

$$R = \frac{S_{si}(t, z) + S_{so}(t, z)}{S_{so}(t, z)} \cdot 100 \tag{9}$$

In bare-rock HVFEs, the heat sink dissipated up to 2% of the on-fault energy density W_{on} (i.e., $z = 0$ m, Figure 7a) and the effects of this heat sink extended in the wall rocks up to ~ 0.3 mm from the sliding surfaces (Figure 7b). The energy sink is effective during stages (ii) and (iii), when measured temperature was constant.

In gouge HVFEs, the dissipation of mechanical energy in plastic deformation processes resulted to be relevant: main contribution could be qualified in comminution because microstructural evidence showed a progressive increase in thickness of the comminuted gouge zone outside the localized PSZ (Figure 6) and shortening continued also during the dynamic weakening stage (Cornelio et al., 2024; Rempe et al., 2017). In modeling the temperature evolution with slip in the gouge experiments (Figure 4), we did not consider the energy sink introduced by comminution and partial or complete amorphization by wear of the gouge particles rims (Hirono et al., 2013; Yund et al., 1990). By neglecting this energy sink, the modeled temperatures resulted systematically
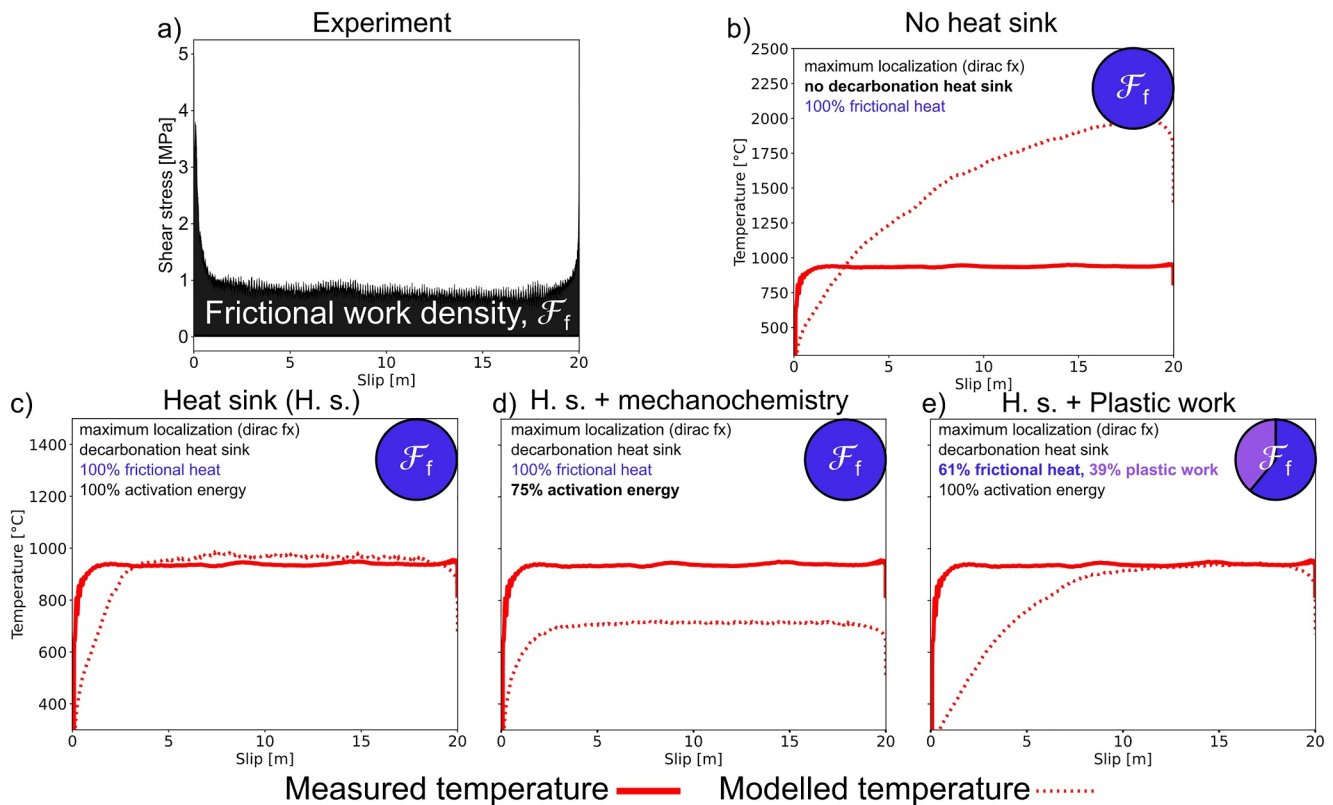
Figure 8. Measured (solid line) and modeled (dashed line) temperature evolution for a bare-rock experiment with a boxcar slip rate function (s1857). (a) The evolution of shear stress with slip during the experiment, with evidenced the area that is the total mechanical energy density $\mathcal{F}_f$ (Equation 8). Modeled (dotted line) and measured (continuous line) temperatures with: (b) no heat sinks (see also Figure S4b in Supporting Information S1), (c) heat sinks as in Figure 3b, (d) heat sinks as in Figure 3b but with the 75% of the activation energy (i.e., 134.9 instead of 179.9 kJ/mol), (e) heat sinks as in Figure 3b but with Taylor-Quinney coefficient β (Equation 2) set to 0.61 instead of 1.

higher than the measured ones. Moreover, comminution and amorphization result in the reduction of the activation energy for chemical reactions (i.e., decarbonation in the case of calcite) due to a lower structural order in the solid reagents (Balaz, 2008; Steinike & Tkáčová, 2000). For this reason, it was necessary to change the assumptions of the temperature models presented here (Figures 3 and 4). The new temperature models for bare-rock (Figure 8) and gouge (Figure 9) HVFEs discussed below include updated energy sinks: (a) energy for plastic deformation processes (e.g., for grain comminution and/or amorphization) by decreasing the Taylor-Quinney coefficient β (Equation 2) and (b) variations in the activation energy of the decarbonation reaction.

Panel a in Figure 8 illustrates the shear stress evolution as a function of slip for bare-rock experiments and the resulting total mechanical work (or frictional work) density $\mathcal{F}_f$. Panels (b) and (c) in Figure 8 show the comparison between modeled and measured temperatures for two cases in which on-fault energy dissipation was solely frictional heat (no energy for plastic deformation processes) without (see also Figure S4 in Supporting Information S1) and with decarbonation energy sinks (100% activation energy), respectively. This comparison further corroborates that the inclusion of decarbonation energy sink yields a constant modeled temperature for bare-rock HVFEs during stage (iii). The corresponding results for gouge experiments are shown in Figure 9. The shear stress evolution as a function of slip and the mechanical work density are depicted in Panel a, while Panels b and c show the comparison between modeled and measured temperatures for frictional heat without (see also Figure S4 in Supporting Information S1) and with decarbonation energy sinks (100% activation energy), respectively. In case of gouge HVFEs, the inclusion of decarbonation energy sink reduces the difference between modeled and measured temperatures. Including the mechanochemical effect by reducing the activation energy for decarbonation to 75% (i.e., 134.9 instead of 179.9 kJ/mol) decreases the modeled temperature during stages (iii) and (iv) to values smaller than the measured temperature in bare-rock HVFEs (Figure 8d), while it reduces the misfit for gouge HVFEs (Figure 9d). Including energy dissipation for plastic deformation processes by using a
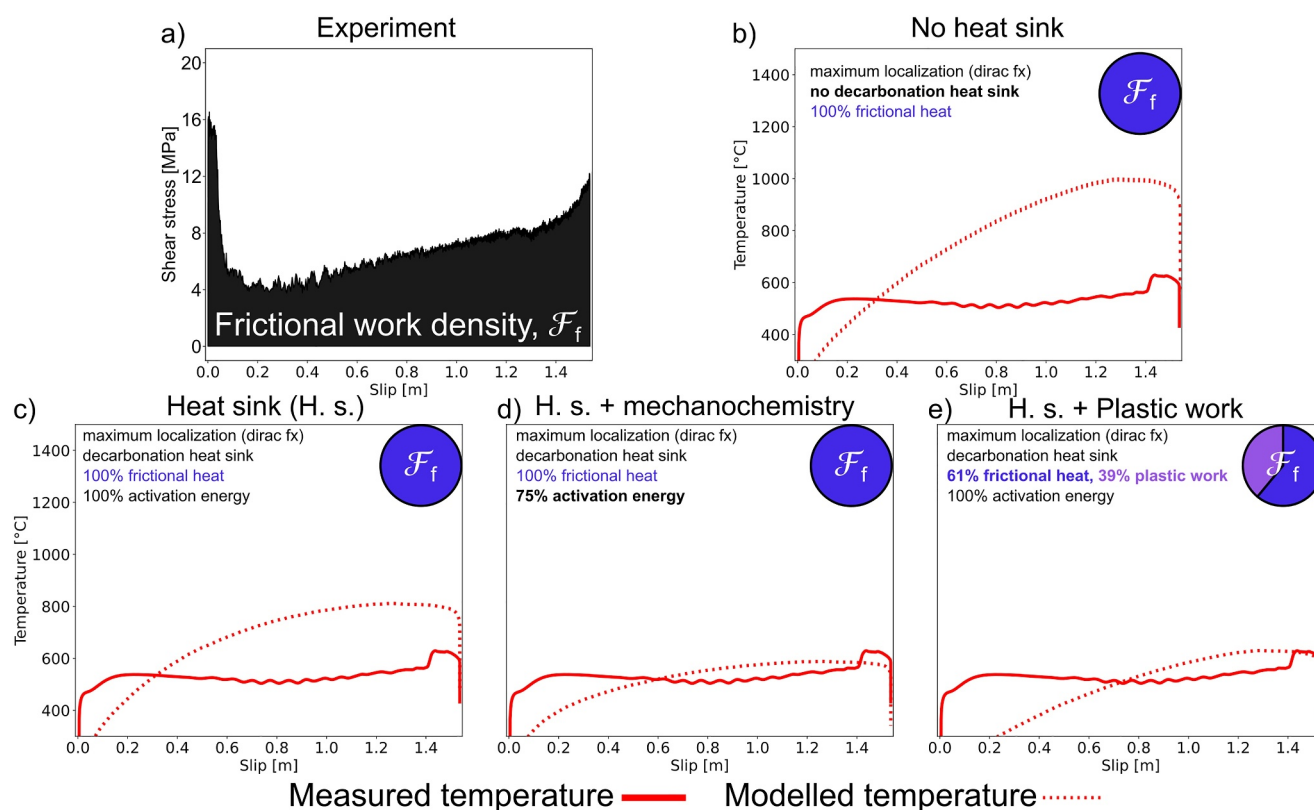
Figure 9. Measured (solid line) and modeled (dashed line) temperature evolution for a fault gouge experiment with regularized Yoffe slip rate function (s1869). (a) The evolution of shear stress with slip during the experiment, with evidenced the area that is the total mechanical energy density $\mathcal{F}_f$ (Equation 8). Modeled (dotted line) and measured (continuous line) temperatures with: (b) no heat sinks (see also Figure S4f in Supporting Information S1), (c) heat sinks as in Figure 4d, (d) heat sinks as in Figure 4d but with the 75% of the activation energy (i.e., 134.9 instead of 179.9 kJ/mol), (e) heat sinks as in Figure 4d but with Taylor-Quinney coefficient β (Equation 2) set to 0.61 instead of 1.

lower value of the Taylor-Quinney coefficient β chosen as 0.61 instead of 1 (Equation 2) for the purpose of attempting a better fit on our data (Taylor & Quinney, 1934) and without considering the mechanochemical effect (i.e., 100% activation energy for decarbonation), yields values of modeled temperature similar to the measured ones, but only at large slip (>5 and >0.7 m for bare-rock and gouge HVFEs, respectively, Figures 8e and 9e). However, the fit is rather poor at small slip values in both bare-rock and gouge HVFEs (Figures 8e and 9e).

Both the reduction of the activation energy for decarbonation reaction and the decrease of the Taylor-Quinney coefficient are presented here as endmember cases, and the choice of the two parameters are done to match as close as possible the measured temperatures. Unfortunately, no estimates of either the decrease in activation energy due to the mechanochemical effects or the increase of energy dissipated for plastic deformation processes are available in the literature at the extreme deformation conditions tested in our laboratory experiments. Moreover, the activation energy of the decarbonation reaction and the Taylor-Quinney coefficient are likely to vary together, since mechanochemical effects require very low grain sizes and therefore energy being dissipated for plastic deformation processes (such as comminution, fracturing, or amorphization), giving rise to any number of possible combinations to constrain the same temperature model against measured temperature. This implies that it is impossible to distinguish the contribution of frictional heat with lower activation energies for the mechanochemical effect from those of energy dissipation for plastic deformation processes. Future work should aim at measuring the real time evolution of temperature and mineral's chemical structure during dynamic weakening experiments, so that it will be possible to verify the occurrence of chemical reactions under extreme disequilibrium conditions.

Despite the experimental and conceptual unknowns, our results highlight a different dissipation of mechanical energy density $\mathcal{F}_f$ depending on the structure of the calcite-bearing fault. On one hand, the faults consisting of

bare-rock contacts dissipate the mechanical energy density $\mathcal{F}_f$ mainly as frictional heat, balanced by the heat sink of the decarbonation reaction. On the other hand, the faults consisting of gouges dissipate the mechanical energy density $\mathcal{F}_f$ as a combination of frictional heat and energy for plastic deformation processes, balanced by the heat sink caused by the decarbonation reaction affected by the mechanochemical effect.

4.4. Implications for Constitutive Behavior During Earthquake Slip

Constitutive laws for seismic slip are proposed to constrain the evolution of shear stress acting on the fault during dynamic breakdown (Bizzarri, 2011 and references therein). Constitutive laws differ in the expression of the analytical dependence of shear stress on different sets of predictive variables, such as slip, slip rate, temperature, or state variables among others. Laboratory experiments might in principle shed light on the analytical dependence of constitutive laws. Unfortunately, the perspective of experimentally calibrating and numerically modeling these laws is limited because only a subset of predictive variables can be measured independently in the laboratory. At the same time, laboratory experiments confirm that multiple predictive variables (e.g., velocity, temperature, and strain) concur to the dynamic weakening of fault materials. In our experiments, the sample contact area was small enough to be considered as an analog to a single point on the slipping natural fault during seismic slip (Nielsen et al., 2016). In fact, the contact areas were hollow circles with 30–50 mm and of 13.9–30 mm inner-outer diameters in bare-rock and gouge HVFEs, respectively. Our results show that the evolution of shear stress during dynamic weakening in stage (ii) is directly controlled by slip rate combined with temperature (Figures 3 and 4). This shows directly what was previously suggested indirectly by combining the microstructural evidences of deformation processes and the modeled temperature from measured shear stress and slip rate (Di Toro et al., 2011; Goldsby & Tullis, 2011; Nielsen et al., 2021; Tisato et al., 2012). Temperature and slip rate are equally important during the initial stages of dynamic breakdown and weakening. However, we also show that temperatures at a lower scale dimension (i.e., the asperity scale) were partly sampled, implying that inhomogeneous temperature distribution on asperities at the onset of slip could not be compared directly with the bulk measurement of shear stress during our experiments to extract the constitutive laws. Future work is necessary to quantitatively investigate the interrelated dependence of shear stress with temperature and slip rate and to generalize the experimental results to general constitutive laws to be applied to physics-based numerical modeling of natural earthquakes.

5. Conclusions

In this work, we perform HVFEs to investigate seismic slip in the case of simulated faults made of calcite-bearing bare-rocks or gouges. Together with normal and shear stress, slip, and slip rate we monitor the temperature evolution of the shearing rock surface or near the localized shear zone in the gouge using an innovative two-color pyrometer. We also perform numerical models of the temperature evolution during simulated seismic slip which include heat sinks from decarbonation reaction across the experimental faults.

Based on the experimental and modeling results reported in this study, we conclude that in the case of bare-rock HVFEs, modeled temperatures agree with measured temperatures at high slip values (>2.5 m, Figure 3), but only by considering the heat sink associated with calcite decarbonation (i.e., compare Figures 3 and 8). At low slip values (<0.3 m), measured temperatures agree with flash temperatures of group of asperities that include from 4% to 6% of the total area of contact. In the case of gouge HVFEs, modeled temperatures (partly) agree with measured temperatures and only by considering the heat sink due to decarbonation and either a decrease of the activation energy for decarbonation or a second energy sink associated with plastic deformation processes (lower Taylor-Quinney coefficient: compare Figure 4 with Figure 9). However, the fit of measured versus modeled temperatures for gouge experiments is achieved only for large slip displacements. Consequently, during dynamic weakening at seismic slip rates (stage ii) the modeled temperatures do not match the measured ones (see Figures 3 and 4). The energy sink due to decarbonation reactions occurs during the dynamic sliding stage (iii) and causes the observed constant temperature. In the case of bare-rocks experiments, on-fault energy density is dissipated as frictional heat and the energy sink due to latent heat of calcite decarbonation. In the case of gouges, on-fault energy dissipation is also due to frictional heat caused by mechanochemical effects and latent heat caused by calcite decarbonation, but these dissipative processes do not allow the fit of the measured temperature values and evolution with slip. The inclusion of energy for plastic deformation processes such as comminution or the reduction of activation energy for calcite decarbonation allow the fit of temperature values at large slip, without reproducing the overall temperature evolution.

Our results confirm that thermally activated processes contribute to on-fault energy dissipation and, therefore, to the total mechanical work dissipated during dynamic sliding at seismic slip values. The observed increase in temperature measured during dynamic weakening confirms the activity of thermally activated weakening processes regardless of the type of fault structure (i.e., bare-rock or gouge). Our results emphasize the need to further investigate temperature changes during HVFEs to better constrain how slip rate and temperature govern dynamic weakening to unravel the constitutive behavior of fault zone materials during seismic slip.

Data Availability Statement

All experimental data and numerical models are available at (Aretusini & Spagnuolo, 2024).

References

Aretusini, S., Meneghini, F., Spagnuolo, E., Harbord, C. W., & Di Toro, G. (2021). Fluid pressurisation and earthquake propagation in the Hikurangi subduction zone. *Nature Communications*, *12*(1), 2481. https://doi.org/10.1038/s41467-021-22805-w

Aretusini, S., Núñez-Cascajero, A., Spagnuolo, E., Tapetado, A., Vázquez, C., & Di Toro, G. (2021). Fast and localized temperature measurements during simulated earthquakes in carbonate rocks. *Geophysical Research Letters*, *48*(9), e2020GL091856. https://doi.org/10.1029/2020GL091856

Aretusini, S., & Spagnuolo, E. (2024). Mechanical data of rotary shear experiments, temperature measurements, and temperature numerical models for the manuscript: "Mechanical energy dissipation during seismic dynamic weakening in calcite-bearing faults" [Dataset]. *Zenodo*. https://doi.org/10.5281/ZENODO.10262683

Aretusini, S., Spagnuolo, E., Dalconi, M. C., Di Toro, G., & Rutter, E. H. (2019). Water availability and deformation processes in Smectite-rich gouges during seismic slip. *Journal of Geophysical Research: Solid Earth*, *124*(11), 10855–10876. https://doi.org/10.1029/2019JB018229

Ashby, M. F., & Verrall, R. A. (1973). Diffusion-accommodated flow and superplasticity. *Acta Metallurgica*, *21*(2), 149–163. https://doi.org/10.1016/0001-6160(73)90057-6

Aubry, J., Passelègue, F. X., Deldicque, D., Girault, F., Marty, S., Lahfid, A., et al. (2018). Frictional heating processes and energy budget during laboratory earthquakes. *Geophysical Research Letters*, *45*(22), 12274–12282. https://doi.org/10.1029/2018GL079263

Aubry, J., Passelègue, F. X., Escartín, J., Gasc, J., Deldicque, D., & Schubnel, A. (2020). Fault stability across the seismogenic zone. *Journal of Geophysical Research: Solid Earth*, *125*(8), e2020JB019670. https://doi.org/10.1029/2020JB019670

Balaz, P. (2008). *Mechanochemistry in nanoscience and minerals engineering*. Springer Science & Business Media.

Barbery, M. R., Chester, F. M., & Chester, J. S. (2021). Characterizing the distribution of temperature and normal stress on flash heated granite surfaces at seismic slip rates. *Journal of Geophysical Research: Solid Earth*, *126*(5), e2020JB021353. https://doi.org/10.1029/2020JB021353

Beeler, N. M., Tullis, T. E., & Goldsby, D. L. (2008). Constitutive relationships and physical basis of fault strength due to flash heating. *Journal of Geophysical Research*, *113*(B1), B01401. https://doi.org/10.1029/2007JB004988

Bernard, P., Lyon-Caen, H., Briole, P., Deschamps, A., Boudin, F., Makropoulos, K., et al. (2006). Seismicity, deformation and seismic hazard in the Western rift of Corinth: New insights from the Corinth rift laboratory (CRL). *Tectonophysics*, *426*(1), 7–30. https://doi.org/10.1016/j.tecto.2006.02.012

Bizzarri, A. (2011). On the deterministic description of earthquakes. *Reviews of Geophysics*, *49*(3), RG3002. https://doi.org/10.1029/2011RG000356

Brantut, N., Schubnel, A., Rouzaud, J.-N. N., Brunet, F., & Shimamoto, T. (2008). High-velocity frictional properties of a clay-bearing fault gouge and implications for earthquake mechanics. *Journal of Geophysical Research*, *113*(B10), 1–18. https://doi.org/10.1029/2007JB005551

Carslaw, H. S., & Jaeger, J. C. (1959). *Conduction of heat in solids*. Clarendon Press.

Chen, J., Niemeijer, A. R., & Spiers, C. J. (2021). Microphysical modeling of carbonate fault friction at slip rates spanning the full seismic cycle. *Journal of Geophysical Research: Solid Earth*, *126*(3), e2020JB021024. https://doi.org/10.1029/2020JB021024

Chen, J., Yang, X., Ma, S., & Spiers, C. J. (2013). Mass removal and clay mineral dehydration/rehydration in carbonate-rich surface exposures of the 2008 Wenchuan Earthquake fault: Geochemical evidence and implications for fault zone evolution and coseismic slip. *Journal of Geophysical Research: Solid Earth*, *118*(2), 474–496. https://doi.org/10.1002/jgrb.50089

Chen, X., Chitta, S. S., Zu, X., & Reches, Z. (2021). Dynamic fault weakening during earthquakes: Rupture or friction? *Earth and Planetary Science Letters*, *575*, 117165. https://doi.org/10.1016/j.epsl.2021.117165

Chiarabba, C., Amato, A., Anselmi, M., Baccheschi, P., Bianchi, I., Cattaneo, M., et al. (2009). The 2009 L'Aquila (central Italy) MW6.3 earthquake: Main shock and aftershocks. *Geophysical Research Letters*, *36*(18), 18308. https://doi.org/10.1029/2009GL039627

Cocco, M., Aretusini, S., Cornelio, C., Nielsen, S. B., Spagnuolo, E., Tinti, E., & Di Toro, G. (2023). Fracture energy and breakdown work during earthquakes. *Annual Review of Earth and Planetary Sciences*, *51*(1), 217–252. https://doi.org/10.1146/annurev-earth-071822-100304

Cocco, M., Spudich, P., & Tinti, E. (2006). On the mechanical work absorbed on faults during earthquake ruptures. *Geophysical Monograph Series*, *170*(1), 237–254. https://doi.org/10.1029/170GM24

Collettini, C., Viti, C., Tesei, T., & Mollo, S. (2013). Thermal decomposition along natural carbonate faults during earthquakes. *Geology*, *41*(8), 927–930. https://doi.org/10.1130/G34421.1

Cornelio, C., Aretusini, S., Spagnuolo, E., Di Toro, G., & Cocco, M. (2024). Multiple seismic slip-rate pulses and mechanical and textural evolution of calcite-bearing fault gouges. *Journal of Geophysical Research: Solid Earth*, *129*(7), 1–20. https://doi.org/10.1029/2024jb029099

Cornelio, C., Spagnuolo, E., Aretusini, S., Nielsen, S., Passelègue, F., Violay, M., et al. (2022). Determination of parameters characteristic of dynamic weakening mechanisms during seismic faulting in cohesive rocks. *Journal of Geophysical Research: Solid Earth*, *127*(7), e2022JB024356. https://doi.org/10.1029/2022JB024356

Cortinovis, S., Fondriest, M., Balsamo, F., Lucca, A., La Valle, F., Pizzati, M., et al. (2024). In-situ rock shattering and strain localization along a seismogenic fault in dolostones (Monte Marine fault, Italian Central Apennines). *Journal of Structural Geology*, *183*, 105144. https://doi.org/10.1016/j.jsg.2024.105144

Covey-Crump, S. J. (1997). The normal grain growth behaviour of nominally pure calcitic aggregates. *Contributions to Mineralogy and Petrology*, *129*(2), 239–254. https://doi.org/10.1007/s004100050335

Demurtas, M. (2018). Seismogenic carbonate-built normal faults: Structure and deformation processes. *Università degli studi di Padova*. Retrieved from https://www.research.unipd.it/handle/11577/3422672

Demurtas, M., Fondriest, M., Balsamo, F., Clemenzi, L., Storti, F., Bistacchi, A., & Di Toro, G. (2016). Structure of a normal seismogenic fault zone in carbonates: The Vado di Corno Fault, Campo Imperatore, Central Apennines (Italy). *Journal of Structural Geology*, *90*, 185–206. https://doi.org/10.1016/j.jsg.2016.08.004

Demurtas, M., Smith, S. A. F., Prior, D. J., Brenker, F. E., & Di Toro, G. (2019). Grain size sensitive creep during simulated seismic slip in nanogranular fault gouges: Constraints from transmission Kikuchi Diffraction (TKD). *Journal of Geophysical Research: Solid Earth*, *124*(10), 10197–10209. https://doi.org/10.1029/2019jb018071

Demurtas, M., Smith, S. A. F., Prior, D. J., Spagnuolo, E., & Di Toro, G. (2019). Development of crystallographic preferred orientation during cataclasis in low-temperature carbonate fault gouge. *Journal of Structural Geology*, *126*, 37–50. https://doi.org/10.1016/j.jsg.2019.04.015

Demurtas, M., Smith, S. A. F., Spagnuolo, E., & Di Toro, G. (2021). Frictional properties and microstructural evolution of dry and wet calcite–dolomite gouges. *Solid Earth*, *12*(3), 595–612. https://doi.org/10.5194/se-12-595-2021

De Paola, N., Holdsworth, R. E., Viti, C., Collettini, C., & Bullock, R. (2015). Can grain size sensitive flow lubricate faults during the initial stages of earthquake propagation? *Earth and Planetary Science Letters*, *431*, 48–58. https://doi.org/10.1016/j.epsl.2015.09.002

Dieterich, J. H., & Kilgore, B. D. (1994). Direct observation of frictional contacts: New insights for state-dependent properties. *Pure and Applied Geophysics*, *143*(1), 283–302. https://doi.org/10.1007/BF00874332

Di Toro, G., Han, R., Hirose, T., De Paola, N., Nielsen, S., Mizoguchi, K., et al. (2011). Fault lubrication during earthquakes. *Nature*, *471*(7339), 494–498. https://doi.org/10.1038/nature09838

Di Toro, G., Niemeijer, A. R., Tripoli, A., Nielsen, S., Di Felice, F., Scarlato, P., et al. (2010). From field geology to earthquake simulation: A new state-of-The-art tool to investigate rock friction during the seismic cycle (SHIVA). *Rendiconti Lincei*, *21*(S1), 95–114. https://doi.org/10.1007/s12210-010-0097-x

Ferri, F., Di Toro, G., Hirose, T., Han, R., Noda, H., Shimamoto, T., et al. (2011). Low-to high-velocity frictional properties of the clay-rich gouges from the slipping zone of the 1963 Vaiont slide, northern Italy. *Journal of Geophysical Research*, *116*(B9), 1–17. https://doi.org/10.1029/2011JB008338

Fondriest, M., Aretusini, S., Di Toro, G., & Smith, S. A. F. (2015). Fracturing and rock pulverization along an exhumed seismogenic fault zone in dolostones: The Foiana Fault Zone (Southern Alps, Italy). *Tectonophysics*, *654*, 56–74. https://doi.org/10.1016/j.tecto.2015.04.015

Fondriest, M., Balsamo, F., Bistacchi, A., Clemenzi, L., Demurtas, M., Storti, F., & Di Toro, G. (2020). Structural Complexity and Mechanics of a Shallow Crustal Seismogenic Source (Vado di Corno Fault Zone, Italy). *Journal of Geophysical Research: Solid Earth*, *125*(9), e2019JB018926. https://doi.org/10.1029/2019JB018926

Gerya, T. (2019). *Introduction to numerical geodynamic modelling*. Cambridge University Press.

Goldsby, D. L., & Tullis, T. E. (2011). Flash heating leads to low frictional earthquake slip rates. *Science*, *334*(6053), 216–218. https://doi.org/10.1126/science.1207902

Goren, L., Aharonov, E., & Anders, M. H. (2010). The long runout of the Heart Mountain landslide: Heating, pressurization, and carbonate decomposition. *Journal of Geophysical Research*, *115*(B10), B10210. https://doi.org/10.1029/2009JB007113

Han, R., Hirose, T., & Shimamoto, T. (2010). Strong velocity weakening and powder lubrication of simulated carbonate faults at seismic slip rates. *Journal of Geophysical Research*, *115*(B3), B03412. https://doi.org/10.1029/2008JB006136

Han, R., Shimamoto, T., Hirose, T., Ree, J.-H., & Ando, J.-I. (2007). Ultralow friction of carbonate faults caused by thermal decomposition. *Science*, *316*(5826), 878–881. https://doi.org/10.1126/science.1139763

Harbord, C., Brantut, N., Spagnuolo, E., & Di Toro, G. (2021). Fault friction during simulated seismic slip pulses. *Journal of Geophysical Research: Solid Earth*, *126*(8), e2021JB022149. https://doi.org/10.1029/2021JB022149

Heaton, T. H. (1990). Evidence for and implications of self-healing pulses of slip in earthquake rupture. *Physics of the Earth and Planetary Interiors*, *64*(1), 1–20. https://doi.org/10.1016/0031-9201(90)90002-F

Hirono, T., Tanikawa, W., Honda, G., Kameda, J., Fukuda, J., & Ishikawa, T. (2013). Importance of mechanochemical effects on fault slip behavior during earthquakes. *Geophysical Research Letters*, *40*(12), 2988–2992. https://doi.org/10.1002/grl.50609

Ida, Y. (1972). Cohesive force across the tip of a longitudinal-shear crack and Griffith's specific surface energy. *Journal of Geophysical Research*, *77*(20), 3796–3805. https://doi.org/10.1029/jb077i020p03796

Kanamori, H., & Brodsky, E. E. (2004). The physics of earthquakes. *Reports on Progress in Physics*, *67*(8), 1429–1496. https://doi.org/10.1088/0034-4885/67/8/R03

Kanamori, H., & Heaton, T. H. (2000). Microscopic and Macroscopic physics of earthquakes. In *Geocomplexity and the physics of earthquakes* (pp. 147–163). American Geophysical Union (AGU). https://doi.org/10.1029/GM120p0147

Lambert, V., & Lapusta, N. (2023). Absolute stress levels in models of low-heat faults: Links to geophysical observables and differences for crack-like ruptures and self-healing pulses. *Earth and Planetary Science Letters*, *618*, 118277. https://doi.org/10.1016/j.epsl.2023.118277

Lee, W.-J., Fanelli, M. F., Cava, N., & Wyllie, P. J. (2000). Calciocarbonatite and magnesiocarbonatite rocks and magmas represented in the system CaO-MgO-CO$_2$-H$_2$O at 0.2 GPa. *Mineralogy and Petrology*, *68*(4), 225–256. https://doi.org/10.1007/s007100050011

Mitchell, T. M., Smith, S. A. F., Anders, M. H., Di Toro, G., Nielsen, S., Cavallo, A., & Beard, A. D. (2015). Catastrophic emplacement of giant landslides aided by thermal decomposition: Heart Mountain, Wyoming. *Earth and Planetary Science Letters*, *411*, 199–207. https://doi.org/10.1016/j.epsl.2014.10.051

Nielsen, S., Di Toro, G., Hirose, T., & Shimamoto, T. (2008). Frictional melt and seismic slip. *Journal of Geophysical Research*, *113*(B1), B01308. https://doi.org/10.1029/2007JB005122

Nielsen, S., Spagnuolo, E., Smith, S. A. F. F., Violay, M., Di Toro, G., & Bistacchi, A. (2016). Scaling in natural and laboratory earthquakes. *Geophysical Research Letters*, *43*(4), 1504–1510. https://doi.org/10.1002/2015GL067490

Nielsen, S., Spagnuolo, E., & Violay, M. (2012). Composite sample mount assembly (SAMOA): The ultimate sample preparation for rotary shear experiments. *INGV Rapporti Tecnici*, 2039–2741.

Nielsen, S., Spagnuolo, E., Violay, M., & Di Toro, G. (2021). Thermal weakening friction during seismic slip: Experiments and models with heat sources and sinks. *Journal of Geophysical Research: Solid Earth*, *126*(5), e2020JB020652. https://doi.org/10.1029/2020JB020652

Niemeijer, A. R., Di Toro, G., Griffith, W. A., Bistacchi, A., Smith, S. A. F., Nielsen, S., et al. (2012). Inferring earthquake physics and chemistry using an integrated field and laboratory approach. *Journal of Structural Geology*, *39*, 2–36. https://doi.org/10.1016/j.jsg.2012.02.018

Noda, H., Kanagawa, K., Hirose, T., & Inoue, A. (2011). Frictional experiments of dolerite at intermediate slip rates with controlled temperature: Rate weakening or temperature weakening? *Journal of Geophysical Research*, *116*(B7), B07306. https://doi.org/10.1029/2010JB007945

Núñez-Cascajero, A., Tapetado, A., Vargas, S., & Vázquez, C. (2021). Optical fiber pyrometer designs for temperature measurements depending on object size. *Sensors*, *21*(2), 1–14. https://doi.org/10.3390/s21020646

Núñez-Cascajero, A., Tapetado, A., & Vazquez, C. (2020). High spatial resolution optical fiber two colour pyrometer with fast response. *IEEE Sensors Journal*, *21*(3), 2942–2950. https://doi.org/10.1109/jsen.2020.3022179

Ohl, M., Plümper, O., Chatzaras, V., Wallis, D., Vollmer, C., & Drury, M. (2020). Mechanisms of fault mirror formation and fault healing in carbonate rocks. *Earth and Planetary Science Letters*, *530*, 115886. https://doi.org/10.1016/j.epsl.2019.115886

Ohnaka, M. (2013). *The physics of rock failure and earthquakes* (1st ed.). Cambridge University Press. https://doi.org/10.1017/CBO9781139342865

Palmer, A. C., & Rice, J. R. (1973). The growth of slip surfaces in the progressive failure of over-consolidated clay. *Proceedings of the Royal Society A: Mathematical, Physical and Engineering Sciences*, *332*(1591), 527–548. https://doi.org/10.1098/rspa.1973.0040

Passelègue, F. X., Aubry, J., Nicolas, A., Fondriest, M., Deldicque, D., Schubnel, A., & Di Toro, G. (2019). From fault creep to slow and fast earthquakes in carbonates. *Geology*, *47*(8), 744–748. https://doi.org/10.1130/G45868.1

Passelègue, F. X., Spagnuolo, E., Violay, M., Nielsen, S., Di Toro, G., & Schubnel, A. (2016). Frictional evolution, acoustic emissions activity, and off-fault damage in simulated faults sheared at seismic slip rates. *Journal of Geophysical Research: Solid Earth*, *121*(10), 7490–7513. https://doi.org/10.1002/2016JB012988

Pozzi, G., De Paola, N., Holdsworth, R. E., Bowen, L., Nielsen, S., & Dempsey, E. D. (2019). Coseismic ultramylonites: An investigation of nanoscale viscous flow and fault weakening during seismic slip. *Earth and Planetary Science Letters*, *516*, 164–175. https://doi.org/10.1016/j.epsl.2019.03.042

Pozzi, G., De Paola, N., Nielsen, S., Holdsworth, R. E., & Bowen, L. (2018). A new interpretation for the nature and significance of mirror-like surfaces in experimental carbonate-hosted seismic faults. *Geology*, *46*(7), 583–586. https://doi.org/10.1130/G40197.1

Pozzi, G., De Paola, N., Nielsen, S. B., Holdsworth, R. E., Tesei, T., Thieme, M., & Demouchy, S. (2021). Coseismic fault lubrication by viscous deformation. *Nature Geoscience*, *14*(6), 437–442. https://doi.org/10.1038/s41561-021-00747-8

Rempe, M., Smith, S. A. F., Mitchell, T. M., Hirose, T., & Di Toro, G. (2017). The effect of water on strain localization in calcite fault gouge sheared at seismic slip rates. *Journal of Structural Geology*, *97*, 104–117. https://doi.org/10.1016/j.jsg.2017.02.007

Rice, J. R. (2006). Heating and weakening of faults during earthquake slip. *Journal of Geophysical Research*, *111*(5), 1–29. https://doi.org/10.1029/2005JB004006

Rodriguez-Navarro, C., Kudlacz, K., & Ruiz-Agudo, E. (2012). The mechanism of thermal decomposition of dolomite: New insights from 2D-XRD and TEM analyses. *American Mineralogist*, *97*(1), 38–51. https://doi.org/10.2138/am.2011.3813

Rodriguez-Navarro, C., Ruiz-Agudo, E., Luque, A., Rodriguez-Navarro, A. B., & Ortega-Huertas, M. (2009). Thermal decomposition of calcite: Mechanisms of formation and textural evolution of CaO nanocrystals. *American Mineralogist*, *94*(4), 578–593. https://doi.org/10.2138/am.2009.3021

Rowe, C. D., Fagereng, Å., Miller, J. A., & Mapani, B. (2012). Signature of coseismic decarbonation in dolomitic fault rocks of the Naukluft Thrust, Namibia. *Earth Planetary Science Letters*, *333–334*, 200–210. https://doi.org/10.1016/j.epsl.2012.04.030

Safarloo, S., Tapetado, A., & Vázquez, C. (2023). Experimental validation of high spatial resolution of two-color optical fiber pyrometer. *Sensors*, *23*(9), 4320. https://doi.org/10.3390/s23094320

Sagy, A., Brodsky, E. E., & Axen, G. J. (2007). Evolution of fault-surface roughness with slip. *Geology*, *35*(3), 283–286. https://doi.org/10.1130/G23235A.1

Schiano Di Cola, V., Cuomo, S., & Severino, G. (2021). Remarks on the numerical approximation of Dirac delta functions. *Results in Applied Mathematics*, *12*, 100200. https://doi.org/10.1016/j.rinam.2021.100200

Siman-Tov, S., Aharonov, E., Sagy, A., & Emmanuel, S. (2013). Nanograins form carbonate fault mirrors. *Geology*, *41*(6), 703–706. https://doi.org/10.1130/G34087.1

Smith, S. A. F. F., Nielsen, S., & Di Toro, G. (2015). Strain localization and the onset of dynamic weakening in calcite fault gouge. *Earth and Planetary Science Letters*, *413*, 25–36. https://doi.org/10.1016/j.epsl.2014.12.043

Spagnuolo, E., Plümper, O., Violay, M., Cavallo, A., & Di Toro, G. (2015). Fast-moving dislocations trigger flash weakening in carbonate-bearing faults during earthquakes. *Scientific Reports*, *5*, 1–11. https://doi.org/10.1038/srep16112

Steinike, U., & Tkáčová, K. (2000). Mechanochemistry of solids - Real structure and reactivity. *Journal of Materials Synthesis and Processing*, *8*(3–4), 197–203. https://doi.org/10.1023/A:1011364110355

Sulem, J., & Famin, V. (2009). Thermal decomposition of carbonates in fault zones: Slip-weakening and temperature-limiting effects. *Journal of Geophysical Research*, *114*(B3), B03309. https://doi.org/10.1029/2008JB006004

Sulem, J., Lazar, P., & Vardoulakis, I. (2007). Thermo-poro-mechanical properties of Clayey gouge and application to rapid fault shearing. *International Journal for Numerical and Analytical Methods in Geomechanics*, *31*(3), 523–540. https://doi.org/10.1002/nag.584

Tapetado, A., Diaz-Alvarez, J., Miguelez, M. H., & Vazquez, C. (2016). Two-color pyrometer for process temperature measurement during machining. *Journal of Lightwave Technology*, *34*(4), 1380–1386. https://doi.org/10.1109/JLT.2015.2513158

Taylor, G. I., & Quinney, H. (1934). The latent energy remaining in a metal after cold working. *Proceedings of the Royal Society of London Series A: Containing Papers of a Mathematical and Physical Character*, *143*(849), 307–326. https://doi.org/10.1098/rspa.1934.0004

Tinti, E., Fukuyama, E., Piatanesi, A., & Cocco, M. (2005). A Kinematic source-time function compatible with earthquake dynamics. *Bulletin of the Seismological Society of America*, *95*(4), 1211–1223. https://doi.org/10.1785/0120040177

Tisato, N., Di Toro, G., De Rossi, N., Quaresimin, M., & Candela, T. (2012). Experimental investigation of flash weakening in limestone. *Journal of Structural Geology*, *38*, 183–199. https://doi.org/10.1016/j.jsg.2011.11.017

Tsutsumi, A., & Shimamoto, T. (1997). High-velocity frictional properties of gabbro. *Geophysical Research Letters*, *24*(6), 699–702. https://doi.org/10.1029/97GL00503

Tullis, T. E. (2015). Mechanisms for friction of rock at earthquake slip rates. In *Treatise on geophysics* (2nd ed., Vol. 4, pp. 139–159). Elsevier B. V. https://doi.org/10.1016/B978-0-444-53802-4.00073-7

Valverde, J. M., Sanchez-Jimenez, P. E., & Perez-Maqueda, L. A. (2015). Limestone calcination nearby equilibrium: Kinetics, CaO crystal structure, sintering and reactivity. *Journal of Physical Chemistry C*, *119*(4), 1623–1641. https://doi.org/10.1021/jp508745u

Veveakis, E., Vardoulakis, I., & Di Toro, G. (2007). Thermoporomechanics of creeping landslides: The 1963 Vaiont slide, northern Italy. *Journal of Geophysical Research*, *112*(F3), 1–21. https://doi.org/10.1029/2006JF000702

Violay, M., Di Toro, G., Nielsen, S., Spagnuolo, E., & Burg, J. P. (2015). Thermo-mechanical pressurization of experimental faults in cohesive rocks during seismic slip. *Earth and Planetary Science Letters*, *429*, 1–10. https://doi.org/10.1016/j.epsl.2015.07.054

Violay, M., Nielsen, S., Spagnuolo, E., Cinti, D., Di Toro, G., & Di Stefano, G. (2013). Pore fluid in experimental calcite-bearing faults: Abrupt weakening and geochemical signature of co-seismic processes. *Earth and Planetary Science Letters*, *361*, 74–84. https://doi.org/10.1016/j.epsl.2012.11.021

Woo, S., Han, R., & Oohashi, K. (2023). Frictional melting mechanisms of rocks during earthquake fault slip. *Scientific Reports*, *13*(1), 12563. https://doi.org/10.1038/s41598-023-39752-9

Yao, L., Ma, S., Chen, J., Shimamoto, T., & He, H. (2018). Flash heating and local fluid pressurization lead to rapid weakening in water-saturated fault gouges. *Journal of Geophysical Research: Solid Earth*, *123*(10), 9084–9100. https://doi.org/10.1029/2018JB016132

Yund, R. A., Blanpied, M. L., Tullis, T. E., & Weeks, J. D. (1990). Amorphous material in high strain experimental fault gouges. *Journal of Geophysical Research*, *95*(B10), 15589–15602. https://doi.org/10.1029/jb095ib10p15589

References From the Supporting Information

Bell, I. H., Wronski, J., Quoilin, S., & Lemort, V. (2014). Pure and pseudo-pure fluid thermophysical property evaluation and the open-source thermophysical property library CoolProp. *Industrial & Engineering Chemistry Research*, *53*(6), 2498–2508. https://doi.org/10.1021/ie4033999

Merriman, J. D., Hofmeister, A. M., Roy, D. J., & Whittington, A. G. (2018). Temperature-dependent thermal transport properties of carbonate minerals and rocks. *Geosphere*, *14*(4), 1961–1987. https://doi.org/10.1130/GES01581.1

U.S. Titanium Industry Inc. (2020). *Titanium alloys—Ti6Al4V grade 5*. AZoM. Retrieved from https://www.azom.com/article.aspx?ArticleID=1547